UPPSALA
UNIVERSITET

Digital Comprehensive Summaries of Uppsala Dissertations from the Faculty of Science and Technology 1159

Biological Insights from Single-Particle Tracking in Living Cells

ARASH SANAMRAD

ACTA
UNIVERSITATIS
UPSALIENSIS
UPPSALA
2014

ISSN 1651-6214
ISBN 978-91-554-8991-5
urn:nbn:se:uu:diva-229342

Dissertation presented at Uppsala University to be publicly examined in lecture hall B42, Uppsala Biomedical Centre, Husargatan 3, Uppsala, Friday, 5 September 2014 at 13:00 for the degree of Doctor of Philosophy. The examination will be conducted in English. Faculty examiner: Professor Achillefs Kapanidis (University of Oxford, Department of Physics, Condensed Matter Physics, Biological Physics).

Abstract

Sanamrad, A. 2014. Biological Insights from Single-Particle Tracking in Living Cells. *Digital Comprehensive Summaries of Uppsala Dissertations from the Faculty of Science and Technology* 1159. 65 pp. Uppsala: Acta Universitatis Upsaliensis. ISBN 978-91-554-8991-5.

Single-particle tracking is a technique that allows for quantitative analysis of the localization and movement of particles. In this technique, trajectories are constructed by determining and connecting the positions of individual particles from consecutive images. Recent advances have made it possible to track hundreds of particles in an individual cell by labeling the particles of interest with photoactivatable or photoconvertible fluorescent proteins and tracking one or a few at a time.

Single-particle tracking can be used to study the diffusion of particles. Here, we use intracellular single-particle tracking and trajectory simulations to study the diffusion of the fluorescent protein mEos2 in living *Escherichia coli* cells. Our data are consistent with a simple model in which mEos2 diffuses normally at 13 $\mu m^2 s^{-1}$ in the *E. coli* cytoplasm. Our approach can be used to study the diffusion of intracellular particles that can be labeled with mEos2 and are present at high copy numbers.

Single-particle tracking can also be used to determine whether an individual particle is bound or free if the free particle diffuses significantly faster than its binding targets and remains bound or free for a long time. Here, we use single-particle tracking in living *E. coli* cells to determine the fractions of free ribosomal subunits, classify individual subunits as free or mRNA-bound, and quantify the degree of exclusion of bound and free subunits separately. We show that, unlike bound subunits, free subunits are not excluded from the nucleoid. This finding strongly suggests that translation of nascent mRNAs can start throughout the nucleoid, which reconciles the spatial separation of DNA and ribosomes with co-transcriptional translation. We also show that, after translation inhibition, free subunit precursors are partially excluded from the compacted nucleoid. This finding indicates that it is active translation that normally allows ribosomal subunits to assemble on nascent mRNAs throughout the nucleoid and that the effects of translation inhibitors are enhanced by the limited access of ribosomal subunits to nascent mRNAs in the compacted nucleoid.

Keywords: single-particle tracking, intracellular diffusion, nucleoid exclusion, transcription-translation coupling, antibiotics

Arash Sanamrad, Department of Cell and Molecular Biology, Computational and Systems Biology, Box 596, Uppsala University, SE-75124 Uppsala, Sweden.

ISSN 1651-6214
ISBN 978-91-554-8991-5
urn:nbn:se:uu:diva-229342 (http://urn.kb.se/resolve?urn=urn:nbn:se:uu:diva-229342)

I often say that when you can measure what you are speaking about, and express it in numbers, you know something about it; but when you cannot measure it, when you cannot express it in numbers, your knowledge is of a meagre and unsatisfactory kind

Lord Kelvin, 1883

List of papers

This thesis is based on the following papers, which are referred to in the text by their Roman numerals.

I English, B.P., Hauryliuk, V.[1], Sanamrad, A.[1], Tankov, S., Dekker, N.H., Elf, J. (2011) Single-molecule investigations of the stringent response machinery in living bacterial cells. *Proc Natl Acad Sci USA*, 108(31):E365–E373

II Sanamrad, A., Persson, F., Lundius, E.G., Fange, D., Gynnå, A.H., Elf, J. (2014) Single-particle tracking reveals that free ribosomal subunits are not excluded from the *Escherichia coli* nucleoid. *Proc Natl Acad Sci USA*, 111(31):11413–11418

Reprints were made with permission from the respective publishers.

[1]V.H. and A.S. contributed equally to this work.

Contents

Abbreviations

CCD	charge-coupled device
DH-PSF	double-helix point spread function
EMCCD	electron-multiplying charge-coupled device
FCS	fluorescence correlation spectroscopy
Fis	factor for inversion stimulation
FP	fluorescent protein
FPALM	fluorescence photoactivated localization microscopy
FRAP	fluorescence recovery after photobleaching
GFP	green fluorescent protein
H-NS	histone-like nucleoid-structuring protein
HU	heat unstable protein
IHF	integration host factor
mRNA	messenger RNA
MSD	mean square displacement
NA	numerical aperture
NAP	nucleoid-associated protein
PALM	photoactivated localization microscopy
rRNA	ribosomal RNA
SPT	single-particle tracking
sRNA	small RNA
STED	stimulated emission depletion
STORM	stochastic optical reconstruction microscopy
tmRNA	transfer-messenger RNA
tRNA	transfer RNA
YFP	yellow fluorescent protein

Introduction

This thesis shows how intracellular single-particle tracking (SPT) can be used to obtain biological insights that cannot easily be obtained using other techniques. The first chapter introduces concepts, organisms, processes, substances and techniques that are important for this thesis. The second chapter shows how we used intracellular SPT to obtain biological insights and the third chapter is a discussion of the future of intracellular SPT.

The central dogma of molecular biology

The central dogma of molecular biology states how sequential information flows between information-carrying biopolymers (see Figure 1). There are three major classes of such biopolymers: DNA, RNA and protein. The central dogma of molecular biology states that information cannot flow from proteins to nucleic acids or other proteins (1).

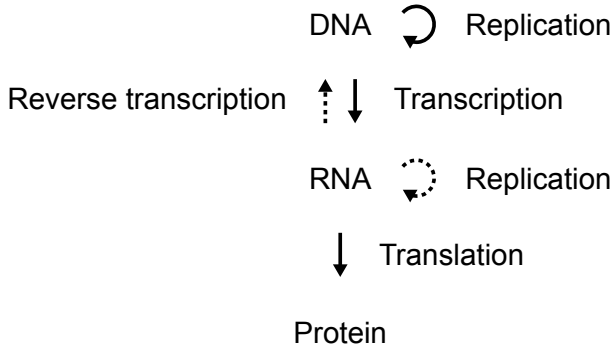

Figure 1. The central dogma of molecular biology. DNA molecules can be replicated from other DNA molecules or reverse-transcribed from RNA molecules. RNA molecules can be replicated from other RNA molecules or transcribed from DNA molecules. Proteins are translated from RNA molecules. RNA replication and reverse transcription occur under special circumstances and are therefore represented as dashed arrows.

DNA molecules store genetic information and consist of nucleotides. Each nucleotide consists of a deoxyribose sugar, a nucleobase and a phosphate group. There are four different nucleobases in DNA molecules and the

genetic information is stored in the sequences of these nucleobases. Most DNA molecules exist as double-stranded helices that are stabilized by hydrogen bonds between the nucleotides and noncovalent interactions between the aromatic nucleobases. The two strands run in opposite directions and store the same biological information. DNA molecules can be replicated from other DNA molecules by enzymes called DNA-dependent DNA polymerases or reverse-transcribed from RNA molecules by enzymes called RNA-dependent DNA polymerases. Eukaryotes store most of their DNA in cell nuclei while prokaryotes store their DNA in the cytoplasm.

RNA molecules can catalyze chemical reactions, regulate gene expression and store genetic information. They consist of four different nucleotides and contain ribose instead of deoxyribose and are therefore less stable than DNA molecules. Unlike DNA molecules, most RNA molecules are single-stranded. There are several types of RNA molecules. Messenger RNA (mRNA) molecules carry sequential information from DNA molecules to protein-making factories called ribosomes. Ribosomal RNA (rRNA) molecules catalyze peptide bond formation in ribosomes. Small RNA (sRNA) molecules can regulate gene expression by binding to mRNA molecules. Transfer RNA (tRNA) molecules deliver amino acids to ribosomes. Transfer-messenger RNA (tmRNA) molecules recycle stalled ribosomes and tag the incomplete nascent polypeptide chains for degradation. Some viruses store their genetic information in RNA molecules. RNA molecules can be replicated from other RNA molecules by enzymes called RNA-dependent RNA polymerases or transcribed from DNA molecules by enzymes called DNA-dependent RNA polymerases.

Proteins can alter the permeabilities of cell membranes to ions and small molecules, bind foreign substances and target them for destruction, bind signaling molecules and induce biochemical responses in the cell, bind small molecules and transport them to other locations, catalyze chemical reactions, generate mechanical forces, provide rigidity, regulate gene expression and transmit signals. Proteins consist of one or multiple chains of amino acid residues that are linked together by peptide bonds. Each of these chains is derived from the condensation of amino acids and each amino acid consists of an α-carbon, an amino group, a carboxyl group and a side chain. The end of the protein with a free carboxyl group is known as the C-terminus or carboxy terminus while the end with a free amino group is known as the N-terminus or amino terminus. The sequence of the amino acid residues in a protein is determined by the nucleotide sequence of the corresponding gene. Proteins are translated from mRNA molecules by ribosomes and most of them fold into specific three-dimensional structures that determine their functions.

Escherichia coli

Escherichia coli (*E. coli*) is a Gram-negative rod-shaped bacterium that elongates along its long axis and divides symmetrically. It is the most widely studied prokaryotic model organism and has many useful characteristics. *E. coli* can be grown easily and can grow both in the absence and presence of oxygen. It has a high growth rate, an easily manipulated genome and relatively simple genetics. Genetic material can be transferred between *E. coli* cells by direct cell-to-cell contact (conjugation), direct uptake of foreign DNA (transformation) or injection of foreign DNA by a bacteriophage virus (transduction). *E. coli* cells are found in the intestines of warm-blooded animals. Most *E. coli* strains are harmless and some may even benefit their hosts by preventing bacterial infections (2) or producing vitamins (3). However, some strains can cause food poisoning in humans by producing toxins.

A typical *E. coli* cell is 2 to 4 μm long and 1 to 2 μm wide (4). Some *E. coli* strains have whip-like tails called flagella that allow them to swim at 14 μm s^{-1} (5). The genome of the *E. coli* strain K-12 consists of 4.6 million base pairs and contains 2584 clusters of genes called operons and 4288 protein-coding genes (6). Protein-coding genes account for 88% of the genome (6) and the average open reading frame encodes 317 amino acids (6). The doubling time of *E. coli* can be as low as 18 min (7) but it takes at least 40 min for an *E. coli* cell to replicate its chromosome (8).

A typical *E. coli* cell contains two chromosomes, 20 million lipids, one million lipopolysaccharides, 1000 mRNA molecules, 60000 rRNA molecules, 200000 tRNA molecules and two million proteins (9). Highly abundant proteins have copy numbers of up to 100000 while 25% and 75% of the cytosolic proteins have copy numbers below 250 and 1160, respectively (10). The mean and median protein copy numbers are 3648 and 526, respectively (10). Protein and RNA molecules account for 55% and 21% of the total dry weight of a typical *E. coli* cell, respectively (9). The water content of a typical *E. coli* cell is 74% (11).

In bacteria, chromosomal DNA occupies only the central part of the cell called the nucleoid. The *E. coli* nucleoid is a discrete, dynamic, helical stiff ellipsoid with low DNA density (12). The nucleoid is radially confined within the cell cylinder and occupies approximately 75% of the cellular space (12). The helical shape arises from the radial confinement, which also directs global nucleoid dynamics (12).

Nucleoid-associated proteins

Most nucleoid-associated proteins (NAPs) can bend, bridge or wrap DNA. Many NAPs can also increase or decrease the amount of transcription. In *E.*

coli, major NAPs include factor for inversion stimulation (Fis), heat unstable protein (HU), histone-like nucleoid-structuring protein (H-NS) and integration host factor (IHF). A typical exponentially growing *E. coli* cell contains 30000 Fis dimers, 10000 H-NS dimers, 20000 HU dimers and 6000 IHF dimers (13). Fis, HU and IHF are distributed throughout the *E. coli* nucleoid (12, 14). In contrast, H-NS forms two compact clusters per chromosome and its deletion leads to a substantial reorganization of the chromosome (14).

Fis binds as a homodimer throughout the *E. coli* genome. It bends the DNA at its binding sites and is involved in DNA recombination, replication and transcription. Fis can activate or repress specific DNA sequences called promoters and can influence DNA supercoiling by regulating the expression of DNA gyrase and DNA topoisomerase I (15). It represses its own expression and affects initiation of chromosome replication at the chromosomal origin (16). Fis colocalizes with RNA polymerase (17) and is most abundant during exponential growth (13).

HU exists as a mixture of hetero- and homodimers in exponentially growing *E. coli* cells (18). It can form multimers consisting of octameric units and regulates genes that respond to DNA damage, acid stress, anaerobic stress and high osmolarity (19). HU introduces flexible bends in DNA molecules at low HU concentrations but stiffens DNA molecules at high HU concentrations (20). HU also affects initiation of chromosome replication at the chromosomal origin (16) and is most abundant during exponential growth (13).

H-NS exists as a hetero- or homodimer. Each subunit consists of a C-terminal DNA-binding domain and an N-terminal dimerization domain. H-NS binds specifically to approximately 250 loci in the *E. coli* genome (21) and can constrain supercoils in DNA (22). It can influence both gene expression and nucleoid structure simultaneously by forming DNA–H-NS–DNA bridges. It is believed that these bridges repress transcription. H-NS colocalizes with RNA polymerase (17) and its overexpression results in highly compacted nucleoids (23). It is most abundant during exponential growth (13).

IHF exists as a heterodimer in *E. coli*. It binds to well-conserved DNA sequences where it introduces U-turns. IHF influences global transcription and can recruit RNA polymerases to promoters (24). It can influence transcription by facilitating interactions between RNA polymerases and regulatory proteins (25). IHF binds to the regulatory regions of stationary-phase genes in *Salmonella enterica* serovar Typhimurium (26). It affects initiation of chromosome replication at the chromosomal origin (16) and is most abundant in early stationary phase (13).

Bacterial polymerases and ribosomes

DNA polymerase III holoenzyme is the most important DNA polymerase in bacteria. It consists of two α subunits with polymerase activity, two β subunits which act as sliding DNA clamps, one γ complex which loads the β clamps onto the DNA, two ε subunits with proofreading activity, two θ subunits which stimulate the ε subunits and two τ subunits which dimerize the α, ε and θ subunits (27). A typical *E. coli* cell contains 10 to 20 DNA polymerase III holoenzymes (28) that synthesize DNA at a rate of around 500 nucleotides per second (29).

The bacterial RNA polymerase holoenzyme consists of two α subunits which are involved in the assembly of the enzyme and interact with specific DNA sequences and regulatory proteins, one β subunit which is involved in the RNA synthesis, one β' subunit which is involved in promoter recognition, one of several σ factors which increase the specificity of the enzyme for promoters and one ω subunit which is involved in the assembly of the enzyme. Each RNA polymerase holoenzyme contains a DNA-binding channel, an RNA exit channel and an active site cleft. A typical *E. coli* cell contains 5000 RNA polymerases (30) that synthesize RNA at a rate of around 28 to 89 nucleotides per second in *E. coli* (31).

The bacterial ribosome consists of a large 50S subunit and a small 30S subunit. The large subunit consists of a 23S RNA subunit, a 5S RNA subunit and 33 proteins while the small subunit consists of a 16S RNA subunit and 21 proteins (32). The large subunit catalyzes peptide bond formation while the small subunit decodes mRNA sequences. Each ribosome contains a decoding center, an mRNA channel, a peptide exit tunnel, a peptidyl transferase center and three tRNA binding sites known as the A site, the P site and the E site. The peptide bonds are formed in the peptidyl transferase center, which is located at the entrance of the peptide exit tunnel. The growing peptide chain passes through and emerges from this tunnel. The tRNA binding sites are located at the interface between the large and the small subunits. Each tRNA molecule binds to the A site after it enters the ribosome, translocates to the P site where it carries the nascent polypeptide chain and then translocates to the E site where is dissociates from the ribosome. A typical *E. coli* cell contains 60000 ribosomes (30) that translate around 12 to 17 amino acids per seconds (33).

Bacterial transcription and translation

Bacterial transcription consists of three stages: initiation, elongation and termination. During initiation, the RNA polymerase binds to a promoter, unwinds the double-stranded DNA and initiates transcription in the presence of nucleoside triphosphate substrates. The transcription complex enters the

elongation stage after synthesizing a short RNA sequence that is 9 to 12 nucleotides long. The RNA polymerase undergoes a significant conformational change during this transition. Termination occurs when the RNA polymerase reaches one or more terminator sequences in the DNA template. In *E. coli*, terminators are either intrinsic, meaning that the nascent transcript is released without the involvement of protein factors, or Rho-dependent, meaning that the termination requires the participation of the transcription termination factor Rho.

Translation consists of four stages: initiation, elongation, termination and ribosome recycling. During initiation, an initiation complex is assembled on the start codon of the mRNA molecule. Amino acids are then added to the nascent polypeptide chain in the elongation cycle, which consists of three steps: aminoacyl-tRNA selection, peptide bond formation and translocation. Termination occurs when a stop codon is translocated into the A site. After the release of the nascent polypeptide chain, the post-termination complex is disassembled into a deacylated tRNA molecule, a large 50S subunit, a small 30S subunit and an mRNA molecule.

In bacteria, translation often starts soon after the ribosome binding site emerges from the RNA exit channel of the RNA polymerase. The transcribing RNA polymerase is then closely followed by translating ribosomes in such a way that the overall transcription elongation rate is tightly controlled by the translation rate (34). This coupling between transcription and translation of nascent mRNAs is important for regulatory mechanisms that respond to the formation of gaps between the transcribing RNA polymerases and the trailing ribosomes. Such gaps may, for example, allow the formation of secondary structures that allow RNA polymerases to proceed through transcription termination sites (35). The gaps may also allow the transcription termination factor Rho to access the nascent mRNAs and terminate transcription (36).

Bacterial 70S ribosomes are formed when large 50S subunits and small 30S subunits assemble on mRNAs. Electron and fluorescence microscopy have revealed that ribosomes are excluded from the *E. coli* nucleoid (14, 30, 37) but this spatial separation of DNA and ribosomes has not yet been reconciled with co-transcriptional translation. The paradox can be reconciled if translation of nascent mRNAs can start throughout the nucleoid before they relocate to the periphery (38). However, this mechanism requires that free ribosomal subunits are not excluded from the nucleoid.

Antibiotics

An antibiotic is a substance that kills or inhibits the growth of microorganisms. Most antibiotics that target the bacterial ribosome inhibit bacterial growth but do not kill the bacteria. Broad-spectrum antibacterial

antibiotics affect a wide range of bacteria while narrow-spectrum antibacterial antibiotics only affect specific types of bacteria. Rifampicin is one of the most broad-spectrum and potent antibiotics and is typically used to treat mycobacterial infections such as leprosy and tuberculosis. It was introduced in the 1960s as a key component in the treatment of tuberculosis. Unfortunately, bacteria quickly develop resistance to rifampicin, which has led to restrictions in its use for the treatment of tuberculosis. Rifampicin forms a very stable complex with the RNA polymerase (39). It binds in a pocket between two domains of the β subunit of the RNA polymerase deep within the main RNA polymerase channel (40). Experimental data indicate that rifampicin directly blocks the path of the elongating RNA transcript when the transcript becomes two to three nucleotides long (40). Rifampicin treatment leads to the depletion of mRNA-bound ribosomal subunits (41). The treatment does not affect the ribosomal RNA, but the large and small ribosomal subunits lose 10 and 20% of their proteins, respectively (41). After rifampicin treatment, the large and small ribosomal subunits sediment at 37S and 25S, respectively (41).

Erythromycin is a clinically important broad-spectrum antibiotic that is often prescribed for patients who are allergic to penicillin. It consists of a 14-membered lactone ring with two sugars attached to it. The complex structure of erythromycin makes it very difficult to produce it synthetically. It is produced by the Gram-positive bacterium *Saccharopolyspora erythraea* and binds to the large subunits of *E. coli* ribosomes with a 1:1 stoichiometry (42, 43). Its binding site has been identified in the central loop of domain V of the 23S rRNA subunit (44). Erythromycin inhibits the initial stage of translation but does not affect elongating ribosomes (45). In addition to inhibiting translation, erythromycin also induces an accumulation of ribosomal precursor particles (46, 47). The precursors of the large ribosomal subunits sediment at 35S and 45S while the precursors of the small ribosomal subunits sediment at 25S (47). Most of these precursors can mature into functional ribosomes at a reduced rate (47). The 25S and 35S particles are highly heterogeneous and contain substoichiometric levels of most of the 30S and 50S proteins (47). In contrast, the 45S particles are highly homogeneous and contain high levels of most of the 50S proteins (47).

Fluorescent proteins

Fluorescent proteins (FPs) absorb light at specific wavelengths and emit light at longer wavelengths. FPs are typically used to label particles of interest. All known FPs consist of an 11-stranded β-barrel and a central α-helix that contains the part of the FPs that absorbs and emits light. An FP is typically characterized by its brightness, emission spectrum, excitation

spectrum, extinction coefficient, pK_a, photostability and quantum yield. The brightness is a measure of how many photons the FP can emit per unit time while the extinction coefficient is a measure of how strongly the FP absorbs light. The photostability is a measure of how many photons the FP can emit before it bleaches while the quantum yield is defined as the ratio of the number of photons emitted over the number of photons absorbed.

The emission spectra of certain FPs can be changed by exposing them to light of specific wavelengths. Photoactivatable FPs irreversibly switch from a dark state to a fluorescent state after exposure to ultraviolet or violet light. Photoconvertible FPs irreversibly switch from one fluorescent state to another while photoswitchable FPs can be switched on and off with light of specific wavelengths. Photoactivatable and photoconvertible FPs have been used to improve fluorescence microscopy (48, 49) and to track hundreds of particles in individual cells (50, 51). Such FPs should be bright, should mature quickly and should not form oligomers.

The first FP was isolated from the jellyfish *Aequorea Victoria* in the 1960s (52). It is known as green fluorescent protein (GFP) and has a major excitation maximum at 395 nm, a minor excitation maximum at 475 nm and an emission maximum at 508 nm (53). The p*K*a value and quantum yield of GFP are 8.1 and 0.77, respectively (53). The gene encoding GFP was cloned and sequenced in the 1990s (54). Shortly after, GFP was successfully expressed in *E. coli* and the roundworm *Caenorhabditis elegans* (55).

mEos2 is a green-to-red monomeric photoconvertible FP that folds efficiently at 37 °C (56). It was developed by introducing seven mutations in the tetrameric FP EosFP (56), which is expressed by the stony coral *Lobophyllia hemprichii* (57). Photoconverted mEos2 molecules can emit thousands of photons before they bleach (14, 58). mEos2 has a weak tendency to oligomerize and can form aggregates when it is used to label membrane proteins (59). The green form of mEos2 has an excitation maximum at 506 nm and an emission maximum at 519 nm (56). The red form of mEos2 has an excitation maximum at 573 nm and an emission maximum at 584 nm (56). The p*K*a values of the green and red forms of mEos2 are 5.6 and 6.4, respectively (56). The quantum yields of the green and red forms of mEos2 are 0.84 and 0.66, respectively (56).

Microscopy

A microscope is an instrument that produces magnified images of samples. There are many different types of microscopes. Electron microscopes produce images by using electromagnetic and electrostatic lenses to focus an electron beam. Light microscopes produce images by using glass lenses to focus visible light while scanning probe microscopes produce images of surfaces by using a physical probe to scan them. The spatial resolution is one

of the most important characteristics of a microscope image and is defined as the minimum distance between two distinguishable objects in the image. Electron microscopy provides very high spatial resolution but requires that cells are fixed or frozen. In contrast, light microscopy provides lower spatial resolution but is compatible with living cells.

Fluorescence microscopy is a form of light microscopy in which particles of interest are labeled with fluorescent molecules and illuminated with light of specific wavelengths. This light is absorbed by the fluorescent molecules which then emit light of longer wavelengths. In fluorescence microscopy, the spatial resolution is proportional to the wavelength of the emission light and is limited to approximately 250 nm. This limit is called the diffraction limit and arises because the points of the samples appear as small disks called Airy disks in the images. The smaller these disks are, the higher the level of detail will be since the disks are less likely to overlap each other.

A number of different approaches have been developed to overcome the diffraction limit. In illumination-based super-resolution microscopy, the resolution is increased by reducing the sizes of the fluorescence spots. In stimulated emission depletion (STED) microscopy, this reduction is achieved by reducing the fluorescence in the outer region of the excitation beam (60, 61). This approach has been used to obtain a spatial resolution of approximately 20 nm (62). In single-molecule super-resolution microscopy, individual fluorescent molecules are stochastically activated, converted or switched on, and imaged until they bleach. The positions of the molecules are then determined by fitting two-dimensional Gaussian functions to their images and are used to construct a super-resolution image. This approach was developed independently by three groups and given the names fluorescence photoactivated localization microscopy (FPALM) (49), photoactivated localization microscopy (PALM) (48) and stochastic optical reconstruction microscopy (STORM) (63). In this approach, the spatial resolution depends on the local densities and localization uncertainties of the imaged particles (see Figure 2). This approach has been used to obtain a spatial resolution of approximately 20 nm (63).

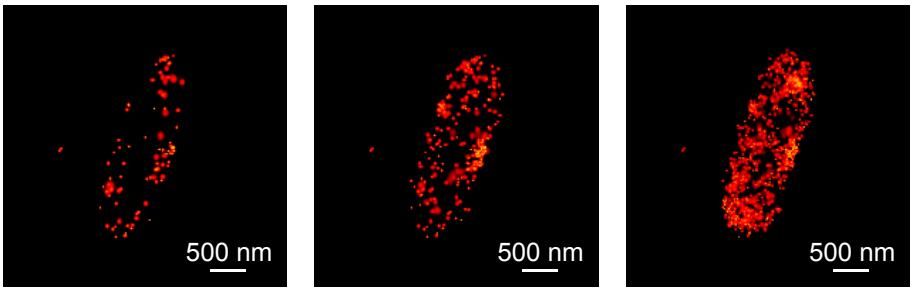

Figure 2. Three single-molecule super-resolution images of mEos2-labeled ribosomal subunits in a living *Escherichia coli* cell. The images are constructed from 100, 300 and 900 independent localizations. The spatial resolution increases with the number of localizations.

Diffusion

Diffusion is the random movement of particles caused by thermal motion. Diffusion processes are typically characterized by their diffusion coefficients and possible deviations from normal diffusion. The diffusion coefficient of a spherical particle in a solution is given by

$$D = \frac{kT}{6\pi\eta r} \qquad \textbf{[1]}$$

where k is the Boltzmann constant, T is the temperature, η is the viscosity of the medium and r is the hydrodynamic radius of the particle. The diffusion coefficient of GFP is 87 $\mu m^2\ s^{-1}$ in solution (64, 65), 30 $\mu m^2\ s^{-1}$ in the cytoplasm and mitochondria of eukaryotic cells (65, 66) and 6 to 8 $\mu m^2\ s^{-1}$ in the cytoplasm of *E. coli* (67, 68). A particle diffuses normally if it performs a simple symmetric random walk and diffuses anomalously if it moves in a different manner. Anomalous diffusion has been observed for chromosomal loci (69) and the cytoskeletal protein FtsZ (51).

In bacteria, diffusion determines the mobility of cytoplasmic particles and sets the limits at which biological reactions can occur. Diffusion is essential for cell division since it promotes a homogenous distribution of cytoplasmic particles and an equal partitioning of cytoplasmic particles between daughter cells. Interestingly, chromosomal loci, plasmids, protein filaments and storage granules diffuse more slowly in bacteria when ATP synthesis is inhibited (70, 71). This observation suggests that ATP-dependent enzymatic activity contributes to the diffusion of particles in living cells (70).

Diffusion is typically studied using fluorescence correlation spectroscopy (FCS) (72), fluorescence recovery after photobleaching (FRAP) (73) or SPT (74). Fluorescence signals from excited particles in very small volumes constantly fluctuate. In FCS, these fluctuations are quantified by calculating

the temporal autocorrelation function. The diffusion coefficient of the particles is then determined by fitting a diffusion model to this function. FCS is typically used to study fast processes on the microsecond timescale. It requires that the average number of fluorescent particles in the observation volume is between 0.1 and 1000, and its spatial resolution is restricted by the diffraction limit.

In FRAP, fluorescent particles are first bleached in a region of interest and the fluorescence intensity in that region is then measured as fluorescent particles move into it. The diffusion coefficient of the particles is then determined by fitting a diffusion model to the fluorescence recovery curve. FRAP is typically used to study slower processes on the millisecond or second timescale. As with FCS, the spatial resolution of FRAP is restricted by the diffraction limit.

Single-particle tracking

SPT is a technique that allows for quantitative analysis of the localization and movement of particles. In this technique, trajectories are constructed by determining and connecting the positions of individual particles from consecutive images (see Figure 3). The positions of the individual particles are typically determined by fitting Gaussian functions to their images. Importantly, single-particle trajectories can be used to determine whether an individual particle is bound or free if the free particle diffuses significantly faster than its binding targets and remains bound or free for a long time (75, 76). Recent advances have made it possible to track hundreds of particles in an individual cell by labeling the particles of interest with photoactivatable or photoconvertible FPs and tracking one or a few at a time (50, 51).

SPT has been used to show that influenza transport consists of three distinct stages and that the virus-containing endocytic compartments mature in three distinct steps (77), that influenza viruses enter cells via multiple endocytic pathways (78) and that the dengue virus enters cells exclusively via clathrin-mediated endocytosis (79). Intracellular SPT has been used to determine transcription elongation rates for individual mRNAs in *E. coli* cells (80), to show that the actin homolog MreB rotates around the long axes of bacterial cells (81-84), to show that the cytoskeletal protein FtsZ displays anomalous diffusion in *E. coli* (51) and to generate a quantitative model of DNA repair in *E. coli* (76).

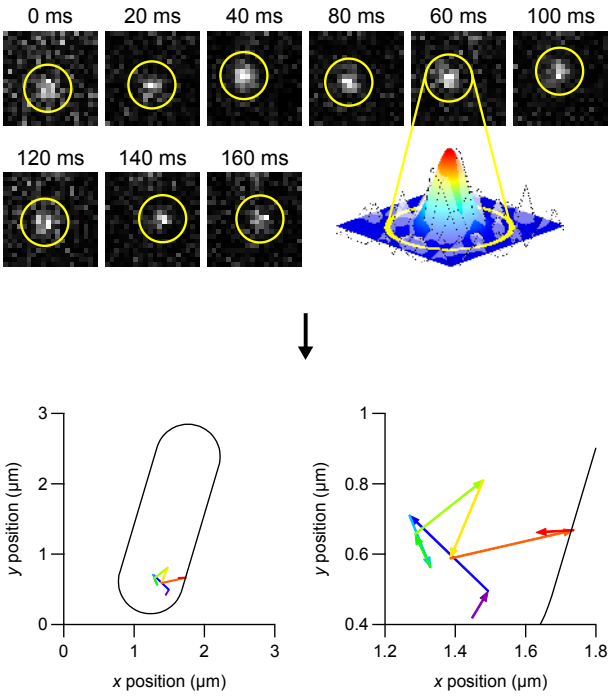

Figure 3. Single-particle tracking of an individual mEos2-labeled free ribosomal subunit in a living *Escherichia coli* cell. A trajectory is constructed by determining and connecting the positions of the subunit from nine consecutive images. The positions of the subunit are determined by fitting Gaussian functions (colored surface) to its images (white surface).

Although particles are usually tracked in two dimensions, they can also be tracked in three dimensions by using astigmatic imaging, biplane imaging or double-helix point spread function (DH-PSF) imaging. In astigmatic imaging, the *z* position of a particle is encoded into the orientation and shape of its image by introducing a weak cylindrical lens into the imaging path (85). In biplane imaging, the positions of a particle are determined by fitting a three-dimensional function to two out-of-focus images of the particle that are obtained by splitting the fluorescence emission (86). In DH-PSF imaging, the *z* position of a particle is encoded into the orientation of its image by a spatial light modulator that converts each fluorescence spot into two fluorescence spots (87). One of the main drawbacks of all of these approaches is that the *z* localization precision is two to three times lower than the *x* and *y* localization precisions (85-87). Another major drawback is that the determined *z* positions differ from the actual *z* positions because of refractive index mismatches between the cytoplasms of the cells and the immersion oils.

Present work

This chapter shows how we used intracellular SPT to obtain biological insights in two investigations. In the first investigation, we used intracellular SPT to study the diffusion of the fluorescent protein mEos2 in the crowded *E. coli* cytoplasm. In the second investigation, we used intracellular SPT to show that free ribosomal subunits are not excluded from the *E. coli* nucleoid. We also showed that free subunit precursors are partially excluded from the compacted nucleoid after translation inhibition.

Diffusion of inert proteins in living cells (paper I)

In this investigation, we used intracellular SPT and trajectory simulations to study the diffusion of the fluorescent protein mEos2 in living *E. coli* cells. Our data are consistent with a simple model in which mEos2 diffuses normally at 13 $\mu m^2\ s^{-1}$ in the *E. coli* cytoplasm. Our approach can be used to study the diffusion of intracellular particles that can be labeled with mEos2 and are present at high copy numbers.

Optical setup

The optical setup was built around an inverted microscope (IX81, Olympus) equipped with a high-numerical-aperture objective (PlanApo N 60x/1.45 Oil, Olympus) and an electron-multiplying charge-coupled device (EMCCD) camera (PhotonMAX: 512B, Princeton Instruments). The microscope included a built-in 1.6x magnification changer and a transmitted light illuminator. The objective is a cylinder containing one or more lenses that collect light from the observed object and focus the light to produce a real image. An objective is typically characterized by its magnification and its numerical aperture (NA), which is a measure of its ability to collect light. It is given by

$$\mathrm{NA} = n \sin\theta \qquad \textbf{[2]}$$

where n is the refractive index of the medium between the objective and the sample and θ is the collecting angle of the objective. The refractive index of the medium is given by

$$n = \frac{c}{v} \quad [3]$$

where c is the speed of light in vacuum and v is the speed of light in the medium. Oil immersion objectives are required to achieve a NA of 1.0 or higher. An inverted microscope is a microscope in which the light source is above the stage while the objectives are below the stage and point upwards.

EMCCD cameras convert incoming photons into electrons and are typically characterized by their cooling temperatures, frame rates, number of pixels, pixel sizes, quantum efficiencies at different wavelengths and readout noises. The quantum efficiency is a measure of the sensitivity of the charge-coupled-device (CCD) sensor and is defined as the probability that an incoming photon generates a photoelectron in the CCD sensor. The readout noise is the noise that arises from the amplification of the photoelectron. The PhotonMAX: 512B EMCCD camera has 512 times 512 16-µm pixels and can achieve a cooling temperature of −80 °C. It has a quantum efficiency at 600 nm of 96% and a readout noise of less than one electron with EM gain enabled. Because of the way EMCCD cameras work, the maximum frame rate depends on the number of horizontal pixel lines in the images. We found that we could image cells at 250 Hz if the images consisted of fewer than 29 horizontal pixel lines. While it is possible to achieve higher frame rates using significantly lower numbers of horizontal pixel lines, we found that it was nearly impossible to fit the cells in such a small number of horizontal pixel lines. We controlled the camera and the microscope with the commercial software MetaMorph (version 7.5, Molecular Devices).

A 405-nm photoconversion laser (Radius 405-50, Coherent) and a 555-nm excitation laser (GCL-150-555, CrystaLaser) were coupled into the microscope using a dichroic mirror (Z405RDC, Chroma Technology). Dichroic mirrors reflect light of specific wavelengths while transmitting light of other wavelengths. The Z405RDC dichroic mirror reflects most of the photoconversion light while transmitting most of the excitation light. The excitation light was filtered by an excitation filter (Z550/20x, Chroma Technology) and modulated by an acousto-optic modulator (AOM-405AF1, IntraAction), which was triggered by the camera through a data acquisition card (PCI-6259, National Instruments). Excitation filters transmit light at a limited range of wavelengths and therefore reduce the illumination of the sample by light of other wavelengths. Acousto-optic modulators use sound waves to deflect light and can be used as fast shutters. We controlled the acousto-optic modulator with the commercial software LabVIEW (version 8.5, National Instruments).

The fluorescence emission was filtered by a dichroic mirror (Z555RDC, Chroma Technology) and two emission filters (HQ565LP and HQ630/140m-2p, Chroma Technology), and imaged by the camera. Emission filters reflect

light of specific wavelengths while transmitting light of other wavelengths. The Z555RDC dichroic mirror and the emission filters reflect most of the excitation light while transmitting most of the emission light. We controlled the photoconversion illumination with a shutter (LS6ZM2, Vincent Associates) and a shutter driver (T132, Vincent Associates). The T132 shutter driver includes two precise timers that we used to control the exposure interval and the delay interval of the LS6ZM2 shutter.

Fluorescence imaging

We grew *E. coli* cells (MG1655) expressing mEos2 from a plasmid derived from the pDendra2-B vector (FP823, Evrogen) overnight at 37 °C in M9 minimal medium supplemented with 0.4% glucose and RPMI 1640 amino acids (R7131, Sigma-Aldrich), diluted them 1:1000 into fresh medium, grew them at 37 °C to an optical density at 600 nm of 0.05 and placed them on a 2.5% agarose pad (SeaPlaque GTG Agarose, Lonza) containing fresh medium. mEos2 was expressed under the control of an inducible promoter which is induced by isopropyl β-D-1-thiogalactopyranoside (IPTG). We found that leakage expression of mEos2 in the absence of IPTG gave a sufficiently high concentration of mEos2 molecules. The cells were imaged at 250 Hz at room temperature (23 ± 2 °C) for up to 3 min in a flow cell (FCS2, Bioptechs). The excitation and photoconversion laser exposure times were 1 and 3 ms, respectively, and the frequencies of the photoconversion pulses were set manually such that, on average, less than one mEos2 molecule was visible at any given time.

The information content of the images is determined by several parameters. The most important parameters are the excitation laser exposure time, the frame rate of the camera, the magnification and the time-averaged laser power densities. A longer excitation laser exposure time will increase the blurriness of the images of the mEos2 molecules, which will make it more difficult to detect them and determine their positions. A lower frame rate will allow the molecules to diffuse longer distances. If it is too low, the positions of the molecules will be nearly uncorrelated, which will make it very difficult to obtain insights from the trajectories. If it is too high, the molecules will appear to be almost stationary, which will also make it very difficult to obtain insights from the trajectories. A higher magnification will give a lower effective pixel size and fewer background photons per pixel, which will reduce the uncertainties of the positions, but it will also increase the number of horizontal pixel lines that are required to image the entire cell, which will reduce the maximum frame rate of the camera.

A higher time-averaged excitation laser power density will increase the number of background photons per pixel and the number of emitted photons. If the time-averaged laser power density is too low, the images of the molecules will consist of very few photons, which will make it very difficult

to detect them and determine their positions. If is too high, the molecules will bleach too quickly, which will reduce the number of points in the trajectories. In addition, a very high time-averaged laser power density can also damage the cells. The time-averaged excitation laser power density is determined by the excitation laser exposure time, the excitation laser power density and the frame rate of the camera.

A higher time-averaged photoconversion laser power density will increase the probability that an mEos2 molecule photoconverts, which will increase the number of mEos2 trajectories that are obtained from each cell, which will improve the statistics, but it will also increase the probability that multiple mEos2 molecules are visible at any given time, which will make it more difficult to construct accurate trajectories. In addition, a very high time-averaged laser power density can also damage the cells. The time-averaged photoconversion laser power density is determined by the photoconversion laser power density and the duration and frequency of the photoconversion pulses.

Image analysis

The images were analyzed with the commercial software DiaTrack (version 3.03, Semasopht). DiaTrack detects images of particles by finding local intensity maxima after the user has specified an intensity threshold. It can determine the positions of the particles by fitting their images with symmetric Gaussian functions after the user has specified the half-width of the Gaussian functions. DiaTrack constructs trajectories by connecting points from consecutive images after the user has specified the maximum allowed *xy* displacement of the particles. To reduce the number of false positives, we only analyzed trajectories that consisted of at least three points.

Cell geometry determination

We approximated the cell geometries as cylinders with hemispherical caps. In this approximation, the geometry is defined by five parameters: the cell angle, the cell length, the cell width, the *x* position of the cell and the *y* position of the cell. Because of the diffraction limit, the geometry of a cell cannot easily be determined with high accuracy from a light microscopy image. However, it is possible to determine the geometry of a cell with high accuracy from the positions of individual particles if the particles are distributed throughout the cell.

To determine the parameters, we plotted all the points in the trajectories and manually drew lines along the long and short axes of the cells (see Figure 4). We calculated the cell angles from the slopes of the long-axis lines, the cell lengths and the *x* and *y* positions of the cells from the end points of the long-axis lines, and the cell widths from the end points of the

short-axis lines. Because of the uncertainties of the positions, a small fraction of the points will always appear to be outside the cells. We took this into account by subtracting four times the mean uncertainty of the x and y positions from the cell lengths and cell widths. We estimated the mean uncertainty of the x and y positions by using an analytical expression for the uncertainty of the x or y position of a stationary particle (88). We determined the cell lengths to be between 1.8 and 3.0 μm and the cell widths to be between 560 and 770 nm.

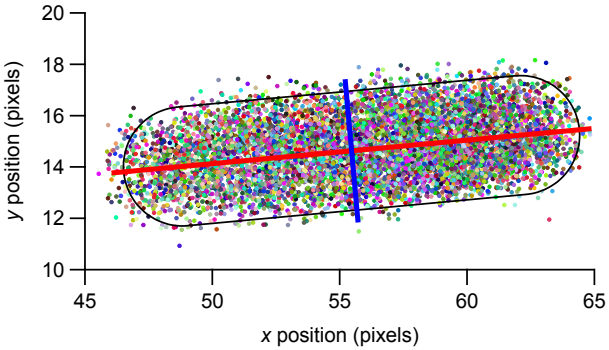

Figure 4. Cell geometry determination from positions of individual mEos2 molecules. The lines are drawn manually along the long and short axes of the *Escherichia coli* cell and are used to determine the geometry of the cell.

Diffusion coefficient determination

If a particle diffuses normally in a volume at a time scale where the confinement is negligible, its diffusion coefficient can be determined by fitting a line to its mean square displacements (MSDs). If this is the case, the diffusion coefficient is given by

$$D = \frac{a}{2n_{\mathrm{d}}} \qquad \textbf{[4]}$$

where a is the slope of the fitted line and n_{d} is the number of dimensions. The diffusion coefficient can also be determined from an individual MSD if the uncertainties of the positions are much smaller than the displacements of the particle. However, if a particle diffuses normally in a volume at a time scale where the confinement is not negligible, its MSDs will not increase linearly and will eventually plateau. The nonlinearity arises because the longer the time interval is, the more likely it is that the displacement of the particle is smaller than it would have been if the particle had not been confined. The MSD plateaus when the next position of a particle no longer depends on its previous position. With infinite statistics, the MSDs at the

plateau are only determined by the geometry of the volume and the uncertainties of the positions. In contrast, the remaining MSDs are also determined by the diffusion coefficient of the particle.

Because the confinement is not negligible for a freely diffusing protein in *E. coli* at the millisecond time scale, we determined the diffusion coefficients of mEos2 by comparing the MSDs of mEos2 with MSDs obtained from trajectory simulations with different diffusion coefficients and manually selecting the diffusion coefficients that gave the best fits. As a control, we determined if the diffusion coefficients depended on the cell geometries by calculating Pearson's correlation coefficient between the cell lengths and the diffusion coefficients. Pearson's correlation coefficient measures linear dependence between two variables X and Y, and is given by

$$r = \frac{\sum_{i=1}^{n}(X_i - X_m)(Y_i - Y_m)}{\sqrt{\sum_{i=1}^{n}(X_i - X_m)^2}\sqrt{\sum_{i=1}^{n}(Y_i - Y_m)^2}} \quad \textbf{[5]}$$

where n is the sample size and X_m and Y_m are the sample means. A value of -1 implies that Y decreases linearly with X while a value of 1 implies that Y increases linearly with X. A value of 0 implies that there is no linear correlation between the variables. We determined the coefficient to be 0.07, that is, the diffusion coefficients of mEos2 did not depend on the cell lengths.

Trajectory simulations

If a particle diffuses normally in a volume at a time scale where the confinement is negligible, the displacements will be normally distributed. If this is the case, trajectories can be simulated by sampling x, y and z displacements from a normal distribution where the standard deviation is given by

$$\sigma_d = \sqrt{2D\tau} \quad \textbf{[6]}$$

where D is the diffusion coefficient and τ is the time interval. However, if a particle diffuses normally in a volume at a time scale where the confinement is not negligible, its displacements will not be normally distributed. If this is the case, the trajectories must be simulated at a shorter time scale so that displacements that move the particle outside the volume can be rejected without changing the overall distribution of the displacements. The displacements at the time scale of interest can then be calculated by adding the corresponding displacements at the shorter time scale. This method will still introduce some errors when the particle is very close to the boundaries

of the volume but these will not give rise to significant errors at the time scale of interest if the sampling period is sufficiently small.

Because the confinement is not negligible for a freely diffusing protein in *E. coli* at the 4-ms time scale, we simulated the trajectories by sampling *x*, *y* and *z* displacements at the 10-μs time scale. All three displacements were resampled if the *xyz* displacement moved the particle outside the cell geometry. Unfortunately, we could not use the starting points of the mEos2 trajectories since some of these were determined to be outside the cells because of the uncertainties of the positions. We solved this problem by sampling the starting points of the trajectories from uniform distributions in the cell geometries.

Ideally, we would have been able to use the distributions of the numbers of points in the mEos2 trajectories. However, when we analyzed the trajectories, we discovered that the cells had been unevenly illuminated. Because of the uneven illumination, mEos2 molecules were not equally likely to be detected throughout the cells. One of the consequences of this artifact was that the mEos2 trajectories were more likely to consist of fewer points if the molecule had diffused very large distances, which gave rise to an apparent slower diffusion at longer timescales (see Figure 5).

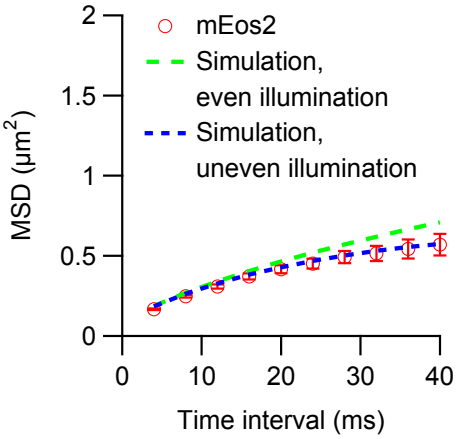

Figure 5. Mean square displacements of mEos2 in a living *Escherichia coli* cell. The cell was imaged at 250 Hz for 3 min on an agarose pad with a laser excitation exposure time of 1 ms. The experimental curve corresponds to more than 1000 trajectories. The simulated mean square displacements (dashed curves) were obtained by simulating more than 10^6 trajectories in a cylinder with hemispherical caps. The simulations correspond to experiments with even (dashed green curve) or uneven (dashed blue curve) illumination. The diffusion coefficient was set to 12.5 $\mu m^2 s^{-1}$. The error bars represent standard errors of the means.

We took this artifact into account by determining the number of points in each trajectory probabilistically. The probability that a trajectory is terminated was given by

$$P_t = C_1 + C_2 p \quad \textbf{[7]}$$

where C_1 and C_2 are constants and p is the long-axis position. The constants were chosen manually for each cell such that mean numbers of points in the trajectories and the spatial distributions of the points were approximately equal for experimental and simulated trajectories. One of the consequences of using this approach is that some the trajectories will consist of fewer than three points. We solved this problem by resimulating each trajectory until it consisted of at least three points.

We took into account the uncertainties of the experimental positions by adding two types of noise to the simulated trajectories. We first added movement noise that was sampled from a normal distribution where the standard deviation was given by

$$\sigma_m = \sqrt{2Dt_e} \quad \textbf{[8]}$$

where t_e is the excitation laser exposure time. This noise was added to account for the uncertainties of the positions which arise from the movement of the molecules during the laser exposures. This noise cannot move the positions of the particles outside the cells and we therefore rejected noise displacements that moved the particles outside the cell geometries. We also took into account the noise that arises from the limited numbers of detected photons by adding noise that was sampled from a normal distribution where the standard deviation was given by the mean uncertainty of the x and y positions of mEos2.

Construction of confidence intervals

A confidence interval is a numerical interval in which a quantity is estimated to lie with a specified probability which is called the confidence level. Each confidence interval consists of a lower confidence limit and an upper confidence limit. These limits can be determined directly if the cumulative distribution function of the estimates of the quantity is known. However, if the cumulative distribution function is unknown, as is usually the case, the confidence limits can instead be estimated using Monte Carlo simulations. In this approach, the quantity is estimated a large number of times and the confidence limits are chosen such that the percentage of the estimates that are larger than the upper confidence limit or smaller than the lower confidence limit is complementary to the confidence level. As an example, if the confidence level is 95%, the lower confidence limit is chosen such that it is larger than 2.5% of the estimates while the upper confidence limit is chosen such that is smaller than 2.5% of the estimates. The estimated confidence intervals converge to the true confidence intervals as the number

of estimates tends to infinity, that is, the accuracy of the estimated confidence intervals depends on the number of estimates. We found that the estimated confidence intervals for the MSDs converged to the true confidence intervals after approximately 1000 estimates.

A quantity is less likely to lie inside every single confidence interval if multiple independent tests are performed. The probability that the quantity lies inside its confidence intervals in every single test is given by

$$P_{\mathrm{n}} = P^{n} \quad \textbf{[9]}$$

where P is the probability that the quantity lies inside its confidence interval in one of the tests and n is the number of tests. As an example, if the confidence level is 95% and eight independent tests are performed, the probability that all the tests will succeed is only 66%. The confidence level for each independent test is therefore given by

$$\gamma_{\mathrm{n}} = \sqrt[n]{\gamma} \quad \textbf{[10]}$$

where γ is the confidence level for the entire test. As an example, a 95% confidence level for one test corresponds to a 99% confidence level for eight independent tests.

We used the confidence intervals for the MSDs to determine whether the MSDs of mEos2 could be explained by a model in which mEos2 diffuses normally at 13 $\mu m^2\ s^{-1}$ in all of the cells. A confidence level of 99% was used for each of the eight individual cells, which corresponds to a confidence level of 95% for all eight cells.

Spatial distributions of ribosomal subunits (paper II)

In this investigation, we used SPT in living *E. coli* cells to determine the fractions of free ribosomal subunits, classify individual subunits as free or mRNA-bound, and quantify the degree of exclusion of bound and free subunits separately. We showed that free subunits are not excluded from the nucleoid. This finding strongly suggests that translation of nascent mRNAs can start throughout the nucleoid, which reconciles the spatial separation of DNA and ribosomes with co-transcriptional translation. We also showed that free subunit precursors are partially excluded from the compacted nucleoid after translation inhibition. This finding indicates that it is active translation that normally allows ribosomal subunits to assemble on nascent mRNAs throughout the nucleoid and that the effects of translation inhibitors are enhanced by the limited access of ribosomal subunits to nascent mRNAs in the compacted nucleoid.

Optical setup

We built the optical setup around an inverted microscope (Eclipse Ti-E, Nikon Instruments) equipped with a high-numerical-aperture objective (Plan Apo VC 100x/1.40, Nikon Instruments) and an EMCCD camera (DU-897E-CS0-#BV, Andor Technology). The microscope included a built-in 1.5x magnification changer and a transmitted light illuminator. The EMCCD camera has 512 times 512 16-µm pixels and can achieve a cooling temperature of −85 °C. It has a quantum efficiency at 600 nm of 97% and a readout noise of less than one electron with EM gain enabled.

We coupled a 405-nm photoconversion laser (Radius 405-50, Coherent) and a 556-nm excitation laser (SDL-556-150T, Shanghai Dream Lasers Technology) into the microscope using a dichroic mirror (Z405RDC, Chroma Technology). The excitation light was filtered by an excitation filter (Z550/20x, Chroma Technology) and modulated by an acousto-optic modulator (AOM-405AF1, IntraAction), which was triggered by the camera through a function generator (DG1022, RIGOL Technologies). The fluorescence emission was filtered by a dichroic mirror (Z555RDC, Chroma Technology) and an emission filter (HQ605/75m, Chroma Technology), and imaged by the camera. We controlled the excitation and photoconversion lasers with two shutters (LS6T2 and LS6ZM2, Vincent Associates) and two shutter drivers (T132 and VMM-D3, Vincent Associates). We controlled the LS6T2 shutter, the camera and the microscope with MetaMorph (version 7.8.1.0, Molecular Devices).

The optical setup was rebuilt during the investigation so that it could also be used in other investigations. In the new setup, a different 405-nm photoconversion laser (MLD 0405-06-01-0100-100, Cobolt) and a 561-nm excitation laser (561L-300-COL-PP, Oxxius) were coupled into the microscope using a different dichroic mirror (ZT405rdc, Chroma Technology). The lasers were modulated by an acousto-optic tunable filter (AOTFnC-400.650-TN, AA OPTOELECTRONIC), which was triggered by the camera through a different function generator (AFG3022C, Tektronix). The fluorescence emission was filtered by a different dichroic mirror (ZT561rdc, Chroma Technology) and two emission filters (ET585/40m and ZET561NF, Chroma Technology), and imaged by the camera.

Camera characterization

Because of the way EMCCD cameras work, the image intensities are stored as number of counts. A baseline offset is added to the output signal from the EMCCD sensor to ensure that each intensity is always a positive number of counts. We determined this offset and the standard deviation of the camera noise to be 100 and 1.9 counts, respectively, by acquiring 200 images with

256 times 256 pixels at 50 Hz with the camera shutter closed and fitting a Gaussian function to the image intensity distribution (see Figure 6).

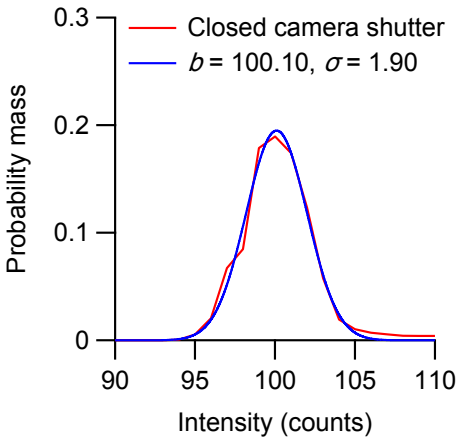

Figure 6. Image intensity distribution obtained from 200 images with 256 times 256 pixels that are acquired at 50 Hz with the camera shutter closed. The experimental distribution (red curve) is fitted with a Gaussian function (blue curve) to determine the baseline offset (b) and the standard deviation of the camera noise (σ).

For a noise-free EMCCD camera that does not have a baseline offset, the image intensity distribution is given by

$$f(c) = e^{-n}\delta(c) + \sqrt{\frac{n}{cm}}e^{-\frac{c}{m}-n}I_1\left(2\sqrt{\frac{cn}{m}}\right) \qquad \textbf{[11]}$$

where c is the intensity in number of counts, n is the mean number of detected photons, m is the multiplication factor and I_1 is the first-order modified Bessel function of the first kind (89). The camera noise is taken into account by convolving this distribution with a normalized Gaussian with a standard deviation corresponding to the standard deviation of the camera noise (89). We determined the multiplication factor to be 12.76 by acquiring two sets of 200 images with 256 times 256 evenly illuminated pixels at 50 Hz with different lamp voltages, flattening the images to correct for any unevenness in the illumination and fitting the model to the image intensity distributions using the Levenberg-Marquardt algorithm (see Figure 7). The Levenberg-Marquardt algorithm is an iterative algorithm that is used to fit a set of observations with a model with one or more unknown parameters. The algorithm can also estimate the standard uncertainties of the parameters of the model. We converted image intensities from counts to number of photons by subtracting the baseline offset and dividing the results by the multiplication factor.

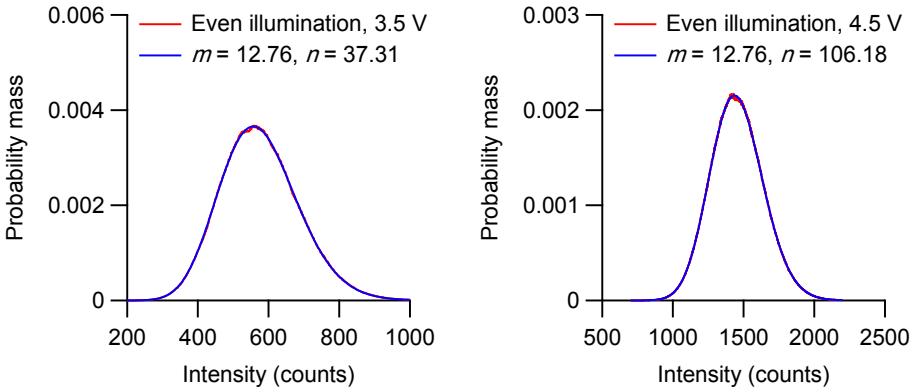

Figure 7. Image intensity distributions obtained from 200 images with 256 times 256 evenly illuminated pixels that are acquired at 50 Hz. The experimental distributions (red curves) are fitted with a model (blue curves) to determine the multiplication factor (*m*). The lamp voltages are 3.5 and 4.5 V, respectively. *n* is the mean number of detected photons.

Strain construction

To obtain trajectories for ribosomal subunits, we constructed *E. coli* strains that express the 50S ribosomal protein L1 and 30S ribosomal protein S2 as fusions to the photoconvertible fluorescent protein mEos2 from their endogenous loci. This means that each L1 or S2 protein is replaced with one L1- or S2-mEos2 protein. We chose to label L1 and S2 since these proteins had previously been successfully labeled with GFP (90) and yellow fluorescent protein (YFP) (30), respectively. Each strain was constructed in four steps: lambda Red-mediated insertion of a DNA fragment encoding mEos2 and chloramphenicol acetyltransferase into the BW25993 chromosome, transfer of the construct to a clean BW25993 background, removal of the chloramphenicol resistance cassette and verification of the construct. Chloramphenicol acetyltransferase is a bacterial enzyme that provides resistance to chloramphenicol. The enzyme prevents chloramphenicol from binding to ribosomes by covalently attaching an acetyl group to it.

The lambda Red-mediated insertion consisted of six steps: synthesis of oligonucleotides for amplification of a DNA fragment encoding mEos2 and chloramphenicol acetyltransferase, amplification and purification of a DNA fragment encoding mEos2 and chloramphenicol acetyltransferase, electroporation of the pKD46 plasmid into BW25993, induction of the recombinase, electroporation of the DNA fragment encoding mEos2 and chloramphenicol acetyltransferase into BW25993 pKD46, and selection of chloramphenicol-resistant cells. The forward primers consisted of three sequences: a 39- or 40-bp sequence from the end of the gene encoding L1 or S2, one codon encoding a glycine linker and a 20- or 24-bp sequence from

the start of the gene encoding mEos2. The reverse primers consisted of two sequences: the reverse complement of a 37- or 40-bp sequence downstream of the gene encoding L1 or S2 and a 20-bp sequence downstream of the gene encoding chloramphenicol acetyltransferase. We amplified the DNA fragments using high-fidelity DNA polymerases to reduce the risk of introducing mutations and purified them using agarose gel purification. The pKD46 plasmid is a low-copy-number temperature-sensitive plasmid that encodes three bacteriophage lambda proteins that mediate homologous recombination (91). The proteins are expressed under the control of an arabinose-inducible promoter to prevent unwanted recombination events (91). We induced the expression of the recombinase in exponentially growing BW25993 pKD46 cells at 30 °C for 2 h 30 min with 0.4% L-(+)-arabinose (A91906, Sigma-Aldrich). The DNA fragments encoding mEos2 and chloramphenicol acetyltransferase were electroporated into the cells and the cells were incubated at 37 °C for 1 h. We selected chloramphenicol-resistant cells by plating the cells on LB-chloramphenicol plates.

The transfer of the construct to a clean BW25993 background consisted of three steps: creation of a P1 phage stock, P1 transduction into a clean BW25993 background and selection of chloramphenicol-resistant cells. P1 is a virus that infects and replicates within *E. coli* cells. It can either integrate into the host genome and coexist with its host or produce new viral particles and escape from the bacterium by lysing it. Importantly, it can capture fragments of the host chromosome when it replicates during its lytic cycle. The captured DNA fragments can then be integrated into the genome of a new host cell if it is infected by the viral particles. This process is called P1 transduction and can be used to transfer a construct to a clean background. This step is important since the lambda Red-mediated insertion can cause unwanted recombination events. We created a P1 stock by incubating the cells and the phages at 37 °C for at least 6 h. The constructs were transferred by incubating BW25993 cells and the phages at 37 °C for 1 h, and chloramphenicol-resistant cells were selected by plating the cells on LB-chloramphenicol plates.

The removal of the chloramphenicol resistance cassette consisted of three steps: electroporation of pCP20 into cells expressing L1- or S2-mEos2, expression of FLP recombinase and verification of loss of pCP20 plasmid and resistance cassette. The pCP20 plasmid is a temperature-sensitive plasmid that encodes a yeast enzyme called FLP recombinase that mediates the deletion of DNA sequences that are flanked by two equally-oriented identical FLP recognition target (FRT) sites (92). It also encodes a bacterial enzyme called β-lactamase that provides resistance to β-lactam antibiotics such as ampicillin (92). The enzyme deactivates the antibiotics by opening a four-atom ring called β-lactam through hydrolysis. The FLP recombinase is expressed under the control of a thermally inducible promoter. We selected ampicillin-resistant transformants at 30 °C and grew the cells overnight at

42 °C. The loss of the pCP20 plasmid and the resistance cassette was verified by plating the cells on LB-ampicillin and LB-chloramphenicol plates.

The construct verification consisted of five steps: synthesis of oligonucleotides for amplification and sequencing of the construct, extraction of chromosomal DNA, amplification of construct, sequencing of construct and sequence alignment. The forward amplification primers consisted of sequences upstream of the gene encoding L1 or S2 while the reverse amplification primers consisted of sequences that were complementary to sequences downstream of the gene encoding mEos2. The chromosomal DNA was extracted by lysing the cells at 95 °C, centrifuging the solution and discarding the pellet. We amplified the constructs using high-fidelity DNA polymerases to reduce the risk of introducing mutations. The constructs were sequenced using a DNA analyzer (3730xl DNA Analyzer, Applied Biosystems). We verified the constructs by aligning the sequences with the expected sequences of the constructs.

A strain expressing the photoconvertible FP Dendra2 was obtained by electroporating a pQE30-derived high-copy-number plasmid encoding Dendra2 into BW25993. The plasmid is unstable due to the lack of *lac* repression in BW25993. We used this strain to verify that rifampicin treatment does not radically change the overall diffusivity in *E. coli* cells.

Strain characterization

Labels may interfere with the functions of the labeled particles and it is therefore important to verify that this is not the case. We verified that this was not the case by monitoring the growth of the strains using a microplate reader (Infinite 200 PRO, Tecan). The cells were grown overnight at 37 °C in M9 minimal medium supplemented with 0.4% glucose and RPMI 1640 amino acids (R7131, Sigma-Aldrich), diluted 1:200 into fresh medium in a microplate (3904, Corning) and grown at 37 °C in the microplate reader. We programmed the microplate reader to measure optical densities at 600 nm every 5 min for 16 h after 1 min of orbital shaking. The growth curves revealed that the labeling did not affect the growth of the cells, showing that the function of the mEos2-labeled ribosomes was not significantly impaired.

Doubling time determination

Exponentially growing cells are typically characterized by their mean doubling time. It is important to determine the mean doubling time since the degree of nucleoid exclusion and the size of the nucleoid may depend on the growth rate of the cells. To determine the mean doubling time, we grew cells at room temperature (23 ± 2 °C) in M9 minimal medium supplemented with

0.4% glucose and RPMI 1640 amino acids (R7131, Sigma-Aldrich) to an optical density at 600 nm of 0.3 and placed them on a 2.5% agarose pad (SeaPlaque GTG Agarose, Lonza) containing fresh medium. The cells were incubated on the pad at room temperature (23 ± 2 °C) for at least 30 min and out-of-focus bright-field images were acquired every 10 min for 1 h in a flow cell (FCS2, Bioptechs). We chose to acquire out-of-focus bright-field images since cells are virtually transparent in in-focus bright-field images. We determined the length of each cell at each time point by fitting an ellipse to a binary image obtained by thresholding the corresponding bright-field image (see Figure 8). The length of each cell was given by the major axis of the corresponding ellipse. We determined the doubling time of each cell by fitting its cell lengths with an exponential growth model using the Levenberg-Marquardt algorithm. In this model, the cell length is given by

$$l(t) = l_0 \times 2^{t/t_d} \quad \textbf{[12]}$$

where t is the time, l_0 is the cell length at time zero and t_d is the doubling time of the cell. We determined the mean doubling time to be 130 ± 10 min (SEM).

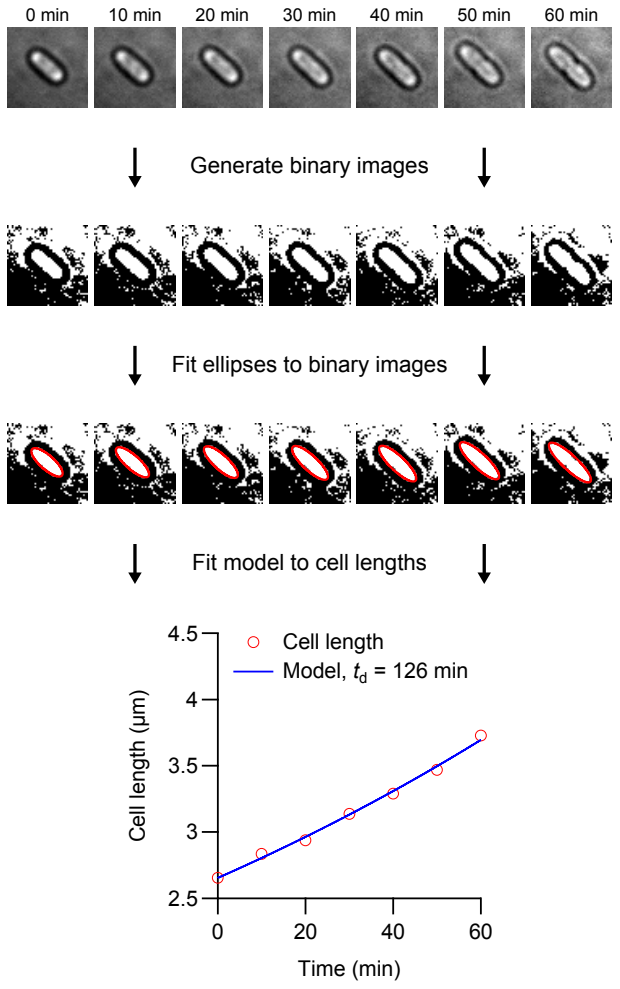

Figure 8. Determination of doubling time of a living *Escherichia coli* cell. The cell is imaged every 10 min for 1 h on an agarose pad. The doubling time is determined by fitting the cell lengths (red circles) with an exponential growth model (blue curve). The cell lengths are determined by fitting ellipses (red ovals) to binary images of the cell. The binary images are obtained by thresholding out-of-focus bright-field images (grayscale images).

Fluorescence imaging

We grew the cells at room temperature (23 ± 2 °C) in M9 minimal medium supplemented with 0.4% glucose and RPMI 1640 amino acids (R7131, Sigma-Aldrich) to an optical density at 600 nm of 0.3 and placed them on a 2.5% agarose pad (SeaPlaque GTG Agarose, Lonza) containing fresh medium. In some of the experiments, we treated the cells with 200 μg ml^{-1} of erythromycin (R5389, Sigma-Aldrich) or rifampicin (R3501, Sigma-Aldrich) for 3 h and placed them on a 2.5% agarose pad containing fresh

medium and 200 μg ml^{-1} of the same antibiotic. We incubated the cells on the pad at room temperature (23 ± 2 °C) for at least 30 min and imaged them at 10, 50 or 200 Hz for 5 min in a flow cell (FCS2, Bioptechs). We used an excitation laser exposure time of 1 ms for freely diffusing Dendra2 proteins and 5 ms for mEos2-labeled ribosomal subunits and HU proteins. The time-averaged laser power densities at the sample were 10 to 100 mW cm^{-2} at 405 nm and 300 W cm^{-2} at 556 or 561 nm for mEos2-labeled ribosomal subunits and HU proteins, and 1 kW cm^{-2} at 561 nm for freely diffusing Dendra2 proteins.

Image analysis

We detected the images of individual proteins and ribosomal subunits with a wavelet segmentation algorithm (93) which consisted of five steps: image smoothing, calculation of the first and second wavelet planes, threshold calculation, binary image generation and particle detection. Each image was smoothed in two different ways by convoluting it with two different matrices. The matrices were given by

$$\mathbf{A} = \mathbf{a}^{\mathrm{T}}\mathbf{a} \qquad [13]$$

$$\mathbf{B} = \mathbf{b}^{\mathrm{T}}\mathbf{b} \qquad [14]$$

where

$$\mathbf{a} = \left[\frac{1}{16} \quad \frac{1}{4} \quad \frac{3}{8} \quad \frac{1}{4} \quad \frac{1}{16}\right] \qquad [15]$$

$$\mathbf{b} = \left[\frac{1}{16} \quad 0 \quad \frac{1}{4} \quad 0 \quad \frac{3}{8} \quad 0 \quad \frac{1}{4} \quad 0 \quad \frac{1}{16}\right] \qquad [16]$$

The first wavelet plane contains most of the noise and is calculated by subtracting the first smoothed image from the raw image. The second wavelet plane contains structures with sizes close to the diffraction limit and is calculated by subtracting the second smoothed image from the first smoothed image. The threshold was given by the standard deviation of the image intensities in the first wavelet plane and the binary image was obtained by thresholding the second wavelet plane. The images of the particles were detected by segmenting the binary image. Each object was counted as a particle if its area was at least five pixels.

We determined the positions of individual proteins and ribosomal subunits by fitting their images with elliptical Gaussian functions using the Levenberg-Marquardt algorithm. In this model, the intensities are given by

$$I(x, y) = he^{-2\left(\frac{(x-x_p)^2}{w_x^2}+\frac{(y-y_p)^2}{w_y^2}\right)} + b \quad \textbf{[17]}$$

where h is the height of the Gaussian, x_p and y_p are the x and y positions of the particle, respectively, w_x and w_y are the x and y widths of the Gaussian, respectively, and b is the sum of the background level and the baseline offset. The parameters of the model can also be determined by maximum-likelihood estimation, that is, by finding the most probable parameter values given the model and the observations. However, such an analysis is slower than fitting using the Levenberg-Marquardt algorithm and does not always produce better results (94). We determined the numbers of photons by calculating the volumes under the fitted Gaussian surfaces. The volume under a Gaussian surface is given by

$$V = \frac{\pi h w_x w_y}{2}. \quad \textbf{[18]}$$

Standard uncertainties of x and y positions were estimated by the fitting algorithm. We reduced the number of false positives by only keeping points that satisfied certain conditions. These conditions allowed us to exclude images of particles with very uncertain positions or weak signals and overlapping images of multiple particles. Each point from cells expressing HupA-, L1- or S2-mEos2 was kept if the fit was successful, the ellipticity was less or equal to 0.5, the number of background photons was greater than zero, the number of photons was at least 100, the standard uncertainties of the x and y positions were less or equal to 40 nm and the x and y widths were between 150 and 450 nm. Each point from cells expressing Dendra2 was kept if the fit was successful, the ellipticity was less or equal to 0.6, the number of background photons was greater than zero, the number of photons was at least 60, the standard uncertainties of the x and y positions were less or equal to 50 nm and the x and y widths were between 150 and 600 nm. The fit was considered to be successful if no errors occurred during the fit. The ellipticity is a measure of how elongated an ellipse is and is given by

$$e = \frac{a - b}{a} \quad \textbf{[19]}$$

where a is the major axis of the ellipse and b is the minor axis of the ellipse. A circle has an ellipticity of 0 and an ellipse that is twice as long as it is wide has an ellipticity of 0.5. A large ellipticity indicates that the image represents more than one particle. The thresholds for the ellipticity, the number of photons, the standard uncertainties and the widths were chosen by analyzing the images and inspecting the distributions of the number of photons, the

standard uncertainties and the widths. It should be noted that the thresholds should be different for images of freely diffusing Dendra2 proteins and images of mEos2-labeled ribosomal proteins and HU proteins. First, the images of the freely diffusing Dendra2 proteins should be larger and more elliptical since Dendra2 diffuses much faster than mEos2-labeled ribosomal subunits and HU proteins. In addition, the number of photons should be lower for the Dendra2 proteins since Dendra2 is 40% less bright than mEos2 (56). Finally, the uncertainties of the x and y positions of the Dendra2 proteins should be larger because of the lower brightness of Dendra2 and the lower magnification that we used to image individual Dendra2 proteins.

Drift correction

Cells slowly move after they are placed on an agarose pad. This movement is called drift and arises from agarose pad evaporation and remaining liquid on the pad surface (95). Drift can distort the spatial distribution of a particle if the cell is imaged for a longer period (see Figure 9). It can also lead to an overestimation of the cell size if the geometry of the cell is determined from the positions of a particle (see Figure 9). Drift can also distort the trajectories of individual particles if the frame rate of the camera is very low.

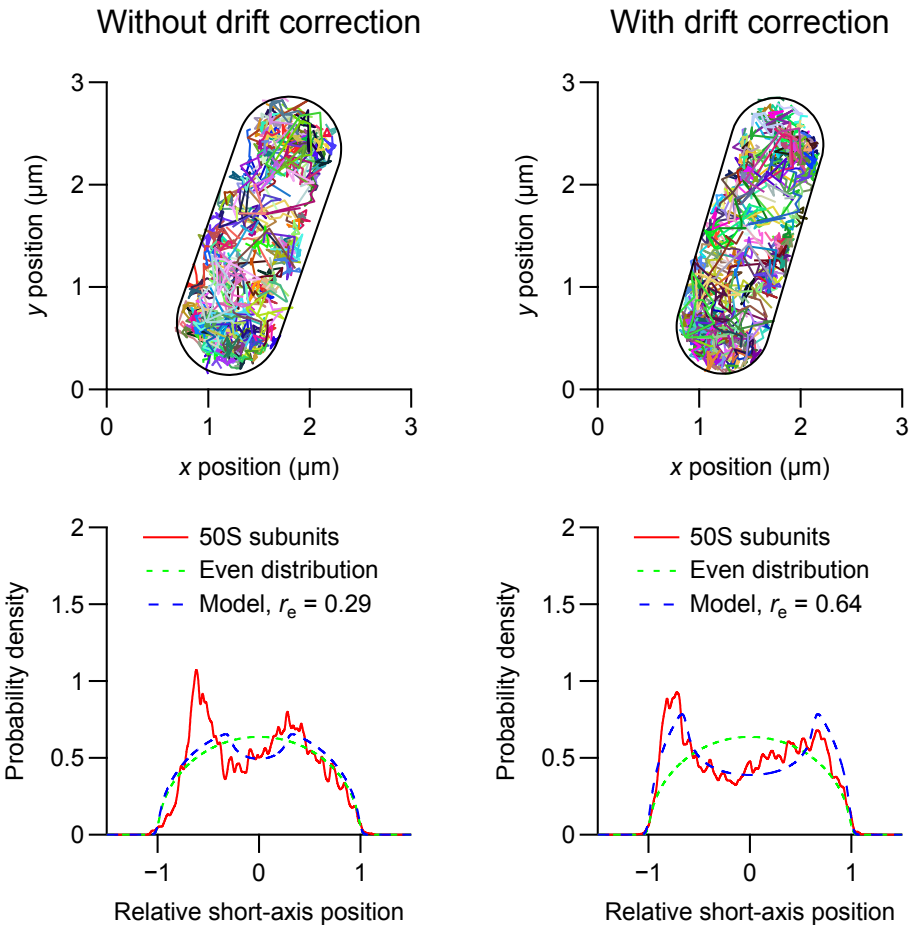

Figure 9. Spatial distribution of large ribosomal subunits in a living *Escherichia coli* cell with and without drift correction. The cell was imaged at 50 Hz for 5 min on an agarose pad with a laser excitation exposure time of 5 ms. The geometry of the cell was determined from the positions of the individual ribosomal subunits. The distributions of the relative short-axis positions of the ribosomal subunits in the cylindrical part of the cell (solid red curves) are fitted with a model for nucleoid-excluded particles (dashed blue curve). Each distribution corresponds to more than 2000 positions. The relative exclusion radius (r_e) is 0 for an evenly distributed particle (dashed green curves) and 1 for a membrane-bound particle.

Drift can be reduced by imaging cells that are closer to the center of the agarose pad, using large agarose pads and waiting until the agarose pad surface is completely dry before placing a coverslip on it (95). However, some amount of drift will always remain (95). We corrected the remaining drift with a drift correction algorithm which consisted of four steps: binary image generation, fitting of ellipses to binary images, drift speed calculation and drift correction. Binary images were generated by thresholding out-of-focus bright-field images acquired before and after fluorescence imaging.

We determined the positions of the cells by fitting ellipses to their binary images. The drift speeds of a cell were given by

$$v_x = \frac{x_2 - x_1}{t_2 - t_1} \quad \textbf{[20]}$$

$$v_y = \frac{y_2 - y_1}{t_2 - t_1} \quad \textbf{[21]}$$

where v_x and v_y are the x and y drift speeds, respectively, x_1 and x_2 are the x positions of the cell before and after the fluorescence imaging, respectively, y_1 and y_2 are the y positions of the cell before and after the fluorescence imaging, respectively, and t_1 and t_2 are the creation times of the out-of-focus bright-field images acquired before and after the fluorescence imaging, respectively. In our case, the drift speeds were typically between 1 and 50 nm min^{-1}. The corrected positions were given by

$$x_c = x_u - nt_f v_x \quad \textbf{[22]}$$

$$y_c = y_u - nt_f v_y \quad \textbf{[23]}$$

where x_c and y_c are the corrected x and y positions, respectively, x_u and y_u are the uncorrected x and y positions, respectively, n is the image number of the image where the particle was detected and t_f is the frame time of the camera.

Cell geometry determination

We approximated the cell geometries as cylinders with hemispherical caps and determined them from out-of-focus bright-field images acquired before the fluorescence imaging or positions of individual ribosomal subunits. The geometry of each cell was determined from the corresponding bright-field image by fitting an ellipse to a binary image obtained from the bright-field image. In this approach, the length and width of each cell were given by the major and minor axis of the corresponding ellipse, respectively. In the second approach, we determined the cell angles by taking advantage of the fact that a poor estimate of the cell angle will lead to an overestimation of the cell volume (see Figure 10). It follows that to determine the cell angle, we simply need to find the cell angle that gives the smallest cell volume. We therefore determined the cell angles by minimizing cell volumes with respect to cell angles. The cell volume was given by

$$V = \pi r^2 \left(h + \frac{4r}{3} \right) \quad \textbf{[24]}$$

where r is the cell radius and h is the cylinder height. A small fraction of the points will always appear to be outside the cells because of the uncertainties of the positions. The length and width of each cell were therefore chosen such that 99.5% of the points were inside the cell. We used this approach for cells expressing L1- or S2-mEos2 since ribosomes have been observed to be present at high copy numbers near the membrane (37) and since we obtained thousands of positions of individual ribosomal subunits from each cell.

The first approach is less accurate because of the inherent difficulty of accurately determining the geometry of a microscopic object from a diffraction-limited bright-field image. On the other hand, the second approach cannot be used if the cells are densely packed or if the fluorescently labeled particles are present at low copy numbers near the membrane. We used the first approach for cells expressing HupA-mEos2 since HU is present at low copy numbers near the membrane. It should be noted that because the first approach is less accurate, particles will appear to be more evenly distributed in the corresponding distributions of the relative positions. We used the cell geometries to determine whether individual ribosomal subunits and HU proteins were in the cylindrical part of a cell and to calculate their relative short-axis positions and standard uncertainties of relative short-axis positions.

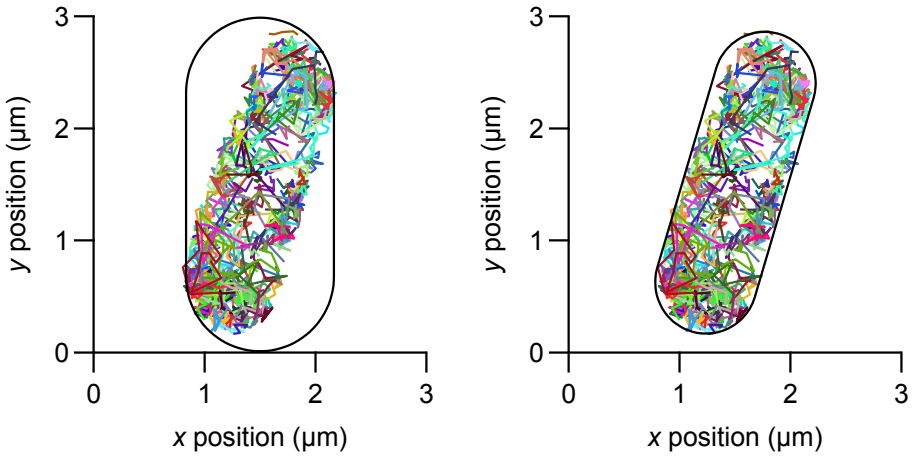

Figure 10. Cell geometry determination from positions of individual ribosomal subunits in a living in *Escherichia coli* cell. A poor estimate of the cell angle will lead to an overestimation of the cell volume.

Trajectory construction

We constructed the trajectories by connecting points from consecutive images. Because of the stochastic nature of diffusion, it is not possible to precisely estimate the apparent diffusion coefficient of a particle from a trajectory consisting of very few points. The precisions of the estimates of the apparent diffusion coefficients are important since they directly affect the classification precisions. The mean precisions can be increased by introducing a threshold for the minimum number of points in a trajectory. However, this threshold will also decrease the total number of trajectories and thereby give poorer statistics. The standard error of the mean of an apparent diffusion coefficient is inversely proportional to the *square root* of the number of points in the trajectory minus one, that is, there is a diminishing return in the precision of the apparent diffusion coefficient with increasing number of points in the trajectory. For example, estimates of apparent diffusion coefficients from trajectories consisting of five points are on average twice as precise as estimates of apparent diffusion coefficients from trajectories consisting of two points. However, estimates of apparent diffusion coefficients from trajectories consisting of 17 points are on average only twice as precise as estimates of apparent diffusion coefficients from trajectories consisting of five points. We decided to keep the trajectories that consisted of at least five points. This threshold allowed us to discard particles with very imprecise estimates of apparent diffusion coefficients without losing almost all of the trajectories.

The maximum allowed *xy* displacement should be chosen carefully. If the maximum allowed *xy* displacement is too small, a bias will arise towards slowly diffusing particles since these have smaller displacements. If the maximum allowed *xy* displacement is too large, trajectories will be terminated prematurely which will lead to poorer statistics. We determined the maximum allowed *xy* displacement by constructing trajectories of ribosomal subunits in rifampicin-treated cells using a maximum allowed *xy* displacement of infinity and generating a cumulative distribution function of the *xy* displacements (see Figure 11). This means that the trajectories were terminated as soon as an image contained more than one point. We chose to analyze the trajectories of the subunits in the rifampicin-treated cells since these display the fastest diffusion. The cumulative distribution function of the *xy* displacements returns the probability that the *xy* displacement of a particle does not exceed a given *xy* displacement. In this case, the cumulative probability of a *xy* displacement of 600 nm over 20 ms was determined to be 0.981 and 0.988 for the large and small ribosomal subunits, respectively, that is, the probability of a ribosomal subunit having an *xy* displacement over 20 ms that is larger than 600 nm is less than 2%. This means that a maximum allowed *xy* displacement of 600 nm over 20 ms will not introduce a significant bias towards slowly diffusing ribosomal particles. We therefore

set the maximum allowed *xy* displacement of ribosomal subunits and HU proteins over 20 ms to 600 nm. Similar analyses were performed for ribosomal subunits that we had tracked at lower frame rates and freely diffusing Dendra2 molecules. We set the maximum allowed *xy* displacements of ribosomal subunits over 100 ms and freely diffusing Dendra2 molecules over 5 ms to 1 and 1.4 µm, respectively.

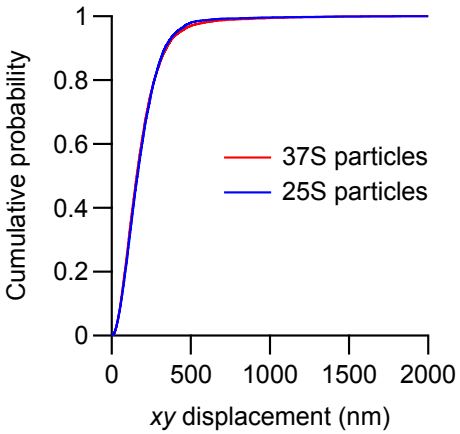

Figure 11. Cumulative distribution functions of *xy* displacements of ribosomal subunits over 20 ms in rifampicin-treated *Escherichia coli* cells. Each curve corresponds to more than 1000 trajectories from eight cells.

Trajectory analysis

We analyzed the trajectories of individual proteins and ribosomal subunits by calculating apparent diffusion coefficients from mean square displacements of individual Dendra2 proteins over 5 ms, individual ribosomal subunits or HU proteins over 20 ms or individual ribosomal subunits over 100 ms. It has been observed that laser illumination can change the distribution of apparent diffusion coefficients (30). We verified that this was not the case by plotting the apparent diffusion coefficients against time (see Figure 12).

Another potential problem is the presence of significant detection bias towards slowly diffusing proteins or ribosomal subunits. We verified the absence of significant detection bias by calculating Pearson's correlation coefficients between apparent diffusion coefficients and numbers of points in trajectories. The coefficients were determined to be between −0.13 and 0.04 for all data sets, showing that there was no significant detection bias towards slowly diffusing proteins or ribosomal subunits.

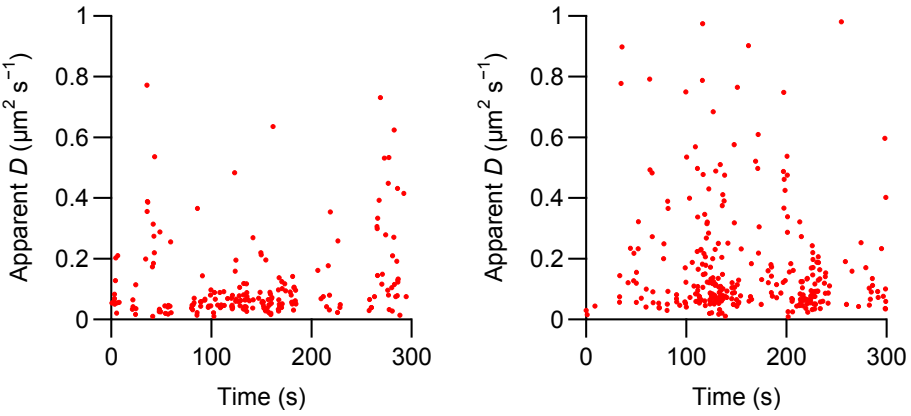

Figure 12. Apparent diffusion coefficients of individual ribosomal subunits in living *Escherichia coli* cells. The cells were imaged at 50 Hz for 5 min on agarose pads with a laser excitation exposure time of 5 ms. The time-averaged laser power densities at the sample were 10 to 100 mW cm^{-2} at 405 nm and 300 W cm^{-2} at 556 nm. Each plot corresponds to more than 200 trajectories from one cell.

Determination of fractions, thresholds and precisions

We determined the fractions of the free ribosomal subunits by treating each distribution of apparent diffusion coefficients in the untreated cells as the sum of an unknown distribution for the mRNA-bound subunits and a known distribution in the rifampicin-treated cells, where all ribosomal subunits are free (41). The fractions were used to determine thresholds for the apparent diffusion coefficients of the individual subunits. We used these thresholds to classify each subunit in the untreated cells as bound or free. It is not possible to completely avoid misclassifications of individual subunits since the distributions of the bound subunits and the distributions of the free subunits overlap. However, we were able to estimate the classification precisions for the individual subunits by classifying the subunits in the rifampicin-treated cells, where all ribosomal subunits are free (41). The classification precisions for the free subunits were given by the fractions of subunits that were classified as free in the rifampicin-treated cells. The classification precisions for the bound subunits are given by

$$p_{\mathrm{b}} = \frac{f_{\mathrm{b}} - f_{\mathrm{f}}(1 - p_{\mathrm{f}})}{f_{\mathrm{b}}} = \frac{1 - f_{\mathrm{f}} - f_{\mathrm{f}}(1 - p_{\mathrm{f}})}{1 - f_{\mathrm{f}}} = \frac{f_{\mathrm{f}}(p_{\mathrm{f}} - 2) + 1}{1 - f_{\mathrm{f}}} \qquad \textbf{[25]}$$

where f_{b} is the fraction of bound ribosomal subunits, f_{f} is the fraction of free ribosomal subunits and p_{f} is the classification precision for the free subunits.

Determination of distributions of relative short-axis positions

To determine the average spatial distributions of the particles, we calculated relative short-axis positions of individual ribosomal subunits and HU proteins. The relative short-axis position of a particle is given by

$$p = \frac{(y_{\mathrm{p}} - y_{\mathrm{c}})\cos\alpha - (x_{\mathrm{p}} - x_{\mathrm{c}})\sin\alpha}{r_{\mathrm{c}}} \qquad \textbf{[26]}$$

where x_{p} and y_{p} are the x and y positions of the particle, respectively, x_{c} and y_{c} are the x and y positions of the cell, respectively, α is the cell angle and r_{c} is the cell radius. We determined the spatial distributions of the particles by representing the relative short-axis positions from the cylindrical parts of the cells by normalized Gaussians with standard deviations corresponding to the standard uncertainties of the relative short-axis positions. These uncertainties were given by

$$\sigma_p = \frac{\sqrt{\sigma_x^2 \sin^2\alpha + \sigma_y^2 \cos^2\alpha}}{r_{\mathrm{c}}} \qquad \textbf{[27]}$$

where σ_x and σ_y are the standard uncertainties of the x and y positions, respectively. We determined the mean standard uncertainties of the relative short-axis positions to be between 0.02 and 0.03 for all data sets.

Modeling of distributions of relative short-axis positions

To be able to quantify the degree of exclusion and estimate changes in the size of the nucleoid, we derived analytical models for the distributions of the relative short-axis positions in the cylindrical parts of the cells. In these models, the particles are either associated with or excluded from a cylinder of unknown radius in the center of the cell. The probability of finding a nucleoid-associated particle at a relative short-axis position is proportional to the height of this cylinder while the probability of finding a nucleoid-excluded particle at a relative short-axis position is proportional to the height of the cell minus the height of this cylinder (see Figure 13). The heights can be calculated with the Pythagorean theorem and the proportionality constants for the nucleoid-associated and nucleoid-excluded particles are given by the inverse of the area of the inner circle and the inverse of the area outside the inner circle, respectively. It follows that the distributions for the nucleoid-associated (f_{a}) and nucleoid-excluded (f_{e}) particles are given by

$$f_a(p) = \frac{2\sqrt{\max\left(r_n^2 - p^2, 0\right)}}{\pi r_n^2} \quad \textbf{[28]}$$

$$f_e(p) = \frac{2\left(\sqrt{\max\left(1 - p^2, 0\right)} - \sqrt{\max\left(r_e^2 - p^2, 0\right)}\right)}{\pi\left(1 - r_e^2\right)} \quad \textbf{[29]}$$

where p is the relative short-axis position, r_e is the relative exclusion radius and r_n is the relative nucleoid radius. We took the uncertainties of the positions into account by convolving these distributions with normalized Gaussians with standard deviations corresponding to the mean standard uncertainties of the relative short-axis positions.

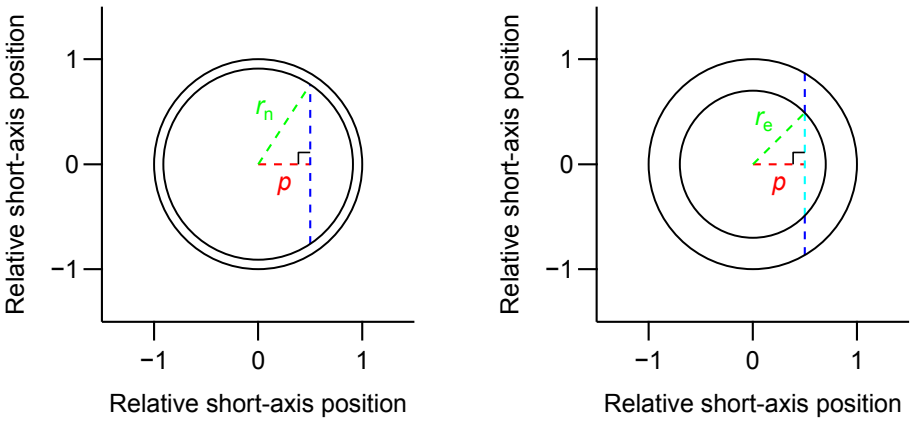

Figure 13. Modeling of distributions of relative short-axis positions. The probability of finding a nucleoid-associated particle at a relative short-axis position (p) is proportional to the height of the inner circle at the relative short-axis position (dashed blue line). The probability of finding a nucleoid-excluded particle at a relative short-axis position is proportional to the height of the cell at the relative short-axis position minus the height of the inner circle at the relative short-axis position (dashed cyan line). r_e is the relative exclusion radius while r_n is the relative nucleoid radius.

The fraction of the space in the cylindrical parts of the cells that a nucleoid-excluded particle is excluded from is given by the square of the relative exclusion radius if the particle is present along the entire lengths of the cylindrical parts of the cells. We used this relation to calculate the fractions of the space in the cylindrical parts of the cells that bound and free ribosomal particles are excluded from. The fraction of the space in the cylindrical parts of the cells that a nucleoid-associated particle occupies is given by the square of the relative nucleoid radius if the nucleoid extends along the entire lengths of the cylindrical parts of the cells. We used this relation to estimate changes in the size of the nucleoid.

Trajectory simulations

We simulated trajectories in spheres or cylinders with hemispherical caps by sampling x, y and z displacements over 10 μs from a normal distribution. All three displacements were resampled if the xyz displacement moved the particle outside the sphere or the cylinder with hemispherical caps. We took the uncertainties of the positions into account by adding normally distributed noise to the x and y positions in the simulated trajectories.

Trajectories were simulated in cylinders with hemispherical caps to determine whether the trajectory classification is robust despite the relatively short trajectories. The bound particles were excluded from 49% of the space in the cylindrical parts of the cells ($r_e = 0.70$) while the free particles were not excluded at all from the nucleoid. We set the diffusion coefficients of the bound and free particles to 0.15 and 0.55 $\mu m^2 s^{-1}$, respectively, to obtain an overlap between the distributions of the apparent diffusion coefficients of the bound and free particles that is similar to the observed overlap between the distributions of the apparent diffusion coefficients of the bound and free ribosomal subunits. The simulated data set consists of the same number of trajectories consisting of the same number of points in the trajectories as one of the experimental data sets. For each point in the simulated trajectories, the uncertainties of the x and y positions were given by the standard uncertainties of the corresponding experimental x and y positions.

We simulated trajectories in spheres to quantify the degree of confinement of bound and free ribosomal subunits. Diffusion coefficients, sphere radii and uncertainties of x and y positions were chosen manually to obtain a good agreement between experimental and simulated MSDs. If a particle is not confined, the sphere diameter should be larger than the average cell width but smaller than the average cell length. It should be noted that the sphere radii for the bound and free subunits are probably over- and underestimated, respectively, since some of the bound subunits are incorrectly classified as free subunits and vice versa.

Concluding remarks

One of the key requirements for intracellular SPT is that the particles of interest can be detected and localized in images. This requirement is typically satisfied by labeling the particles of interest with FPs. However, FPs may interfere with the functions of the labeled particles and can therefore not always be used. One possible solution to such problems is to label the particles of interest with small organic dyes in vitro and introduce them into the cells using electroporation (96). Because organic dyes are generally more photostable than FPs, this approach will also increase the average number of points in the trajectories. The main drawbacks of this approach are that the electroporation can damage the cells, that the particles may bind nonspecifically to the outer cell membrane and that unreacted dye molecules may be introduced into the cells (97).

In the first investigation, we used intracellular SPT and trajectory simulations to study the diffusion of the fluorescent protein mEos2 in living *E. coli* cells. Our approach can be used to study the diffusion of intracellular particles that can be labeled with mEos2 and are present at high copy numbers. If the particles are present at low copy numbers, our approach can be modified to remove the requirement that the particle is present at high copy numbers. Instead of simulating all the trajectories in one cell geometry, each trajectory can be simulated in the cell geometry that is associated with the corresponding experimental trajectory. In addition, the cell geometries can be determined from images acquired before the fluorescence imaging. Ideally, the geometry of each cell should be determined by fitting the corresponding image with a model that takes into account the optical properties of the image. If such a model cannot be obtained, the geometry of each cell can be determined by, for example, fitting an ellipse to a binary image obtained by thresholding the corresponding image.

In the second investigation, we used SPT in living *E. coli* cells to determine the fractions of free ribosomal subunits, classify individual subunits as free or mRNA-bound, and quantify the degree of exclusion of bound and free subunits separately. Our approach can be used to analyze the localization of other bound and free particles separately if the fraction of the free particles can be determined and the free particles diffuse significantly faster than their binding targets and remain bound or free for a long time. The requirement that the free particles diffuse significantly faster than their

binding targets is likely to be satisfied for particles that bind to DNA molecules, mRNA molecules and the membrane.

Intracellular SPT can also be used to determine how long an individual particle is bound to its binding target if the free particle diffuses significantly faster than its binding target and the particle binds to, remains bound to and dissociates from its binding target before it bleaches (76). The frame rate should be chosen carefully to obtain such trajectories. A lower frame rate will reduce the number of frames in which the particle is bound. This reduction will make it more difficult to detect binding events and reduce the precision with which the binding times are determined. A higher frame rate will reduce the probability that the particles of interest bind to, remain bound to and dissociate from their binding targets before they bleach.

To date, most of the biological insights from intracellular SPT have been obtained from SPT in living *E. coli* cells. Nonetheless, biological insights have also been obtained from SPT in the Gram-negative bacterium *Caulobacter crescentus* (81) and the Gram-positive bacterium *Bacillus subtilis* (82, 83). Importantly, there are no major issues that prevent the widespread use of SPT in other bacteria. However, there are at least two major issues that prevent the widespread use of SPT in eukaryotic cells. The first issue is that the particles of interest can diffuse out of the focal plane, which can make it very difficult to obtain trajectories consisting of many points. The second issue is the presence of out-of-focus fluorescence, which makes it difficult to detect and localize the particles of interest. This issue can be addressed by illuminating horizontal sections of the cells with a thin horizontal light sheet close to the sample surface (98).

Swedish summary

Molekylärbiologins centrala dogm anger hur sekvensinformation överförs mellan informationsbärande biopolymerer. Det finns tre huvudklasser av sådana biopolymerer: DNA, RNA och protein. Molekylärbiologins centrala dogm anger att information inte kan överföras från proteiner till nukleinsyror eller andra proteiner. DNA-molekyler lagrar genetisk information och kan replikeras från andra DNA-molekyler av enzymer som kallas DNA-beroende DNA-polymeraser. mRNA-molekyler överför sekvensinformation från DNA-molekyler till proteinfabriker som kallas ribosomer. RNA-molekyler kan transkriberas från DNA-molekyler av enzymer som kallas DNA-beroende RNA-polymeraser. Proteiner translateras från mRNA-molekyler av ribosomer och de flesta veckar sig till specifika tredimensionella strukturer som bestämmer deras funktioner.

Escherichia coli (*E. coli*) är en gramnegativ stavformad bakterie som växer längs sin långaxel och delar sig symmetriskt. Den är den mest studerade prokaryota modellorganismen och har många användbara egenskaper. *E. coli* kan enkelt odlas och kan odlas både med och utan syre. Den har en hög tillväxthastighet, ett genom som kan manipuleras enkelt och relativt enkel genetik. I bakterier finns kromosomalt DNA enbart i den centrala delen av cellen som kallas nukleoiden. *E. coli*-nukleoiden är en dynamisk, helixformad, stel välavgränsad ellipsoid med låg DNA-densitet som upptar ungefär 75 % av cellens volym.

I bakterier startar proteinsyntesen ofta strax efter att ribosombindingsstället kommer ut ur RNA-polymerasets RNA-utgångskanal. Translaterande ribosomer följer därefter det transkriberande RNA-polymeraset på ett sätt så att den övergripande transkriptionselongeringshastigheten snävt kontrolleras av translationshastigheten. Den här kopplingen mellan transkription och translation av gryende mRNA:n är viktig för regleringsmekanismer som är känsliga för bildandet av luckor mellan de transkriberande RNA-polymeraserna och de translaterande ribosomerna. Elektron- och fluorescensmikroskopi har visat att ribosomer är uteslutna från *E. coli*s nukleoid men den här separationen mellan DNA och ribosomer har ännu inte förlikats med kotranskriptionell proteinsyntes. Paradoxen kan lösas om translation av gryende mRNA:n kan starta i hela nukleoiden innan de hamnar i periferin. Den här mekanismen kräver dock att fria ribosomala subenheter inte är uteslutna från nukleoiden.

Ett antibiotikum är ett ämne som dödar mikroorganismer eller hämmar deras tillväxt. Rifampicin är ett antibiotikum som i regel används för att behandla mykobakteriella infektioner som exempelvis spetälska och tuberkulos. Antibiotikumet bildar ett väldigt stabilt komplex med RNA-polymeraset. Rifampicin-behandling leder till att alla ribosomala subenheter blir fria. Erytromycin är ett antibiotikum som ofta ordineras till patienter som är allergiska mot penicillin. Antibiotikumet hämmar det första steget i proteinsyntesen men påverkar inte elongerande ribosomer. Erytromycin-behandling leder dessutom till en ansamling av ribosomala prekursorpartiklar.

Fluorescenta proteiner absorberar ljus vid specifika våglängder och avger ljus vid längre våglängder. De används i regel för att märka partiklar. Vissa fluorescenta proteiners emissionsspektra kan ändras om de utsätts för ljus med specifika våglängder. Fotoaktiverbara fluorescenta proteiner övergår irreversibelt från ett mörkt tillstånd till ett fluorescent tillstånd efter att de har utsatts för ultraviolett eller violett ljus. Fotoomvandlingsbara fluorescenta proteiner övergår i stället irreversibelt från ett fluorescent tillstånd till ett annat. mEos2 är ett grönt-till-rött monomert fotoomvandlingsbart fluorescent protein som veckar sig effektivt vid 37 °C. Fotoomvandlade mEos2-molekyler kan avge tusentals fotoner innan de bleks.

Diffusion är partiklars slumpmässiga rörelser som orsakas av termisk rörelse. Diffusionsprocesser karakteriseras i regel av sina diffusionskoefficienter och möjliga avvikelser från normal diffusion. En partikel diffunderar normalt om den utför en enkel symmetrisk slumpvandring och diffunderar anormalt om den rör sig på något annat sätt. Anormal diffusion har observerats för kromosomala lokus och cytoskelettproteinet FtsZ. I bakterier avgör diffusion hur cytoplasmatiska partiklar rör sig och hur snabbt biologiska reaktioner kan ske.

Spårning av enskilda partiklar är en teknik som möjliggör kvantitativ analys av partiklars lokalisering och rörelse. I den här tekniken konstrueras trajektorier genom att bestämma och ansluta enskilda partiklars positioner från på varandra följande bilder. De enskilda partiklarnas positioner bestäms i regel genom att anpassa gaussfunktioner till deras bilder. Enskilda partiklars trajektorier kan användas för att avgöra om en enskild partikel är bunden eller fri om partikeln diffunderar betydligt snabbare när den är fri och är bunden eller fri under en längre tid. Nya framsteg har gjort det möjligt att spåra hundratals partiklar i en enskild cell genom att märka partiklarna med fotoaktiverbara eller fotoomvandlingsbara fluorescenta proteiner och spåra en eller några få i taget.

Inerta proteiners diffusion i levande celler (delarbete I)

I delarbete I använde vi intracellulär spårning av enskilda partiklar och trajektoriesimuleringar för att studera det fluorescenta proteinet mEos2:s diffusion i levande *E. coli*-celler. Vår data överensstämmer med en enkel modell där mEos2 diffunderar normalt i 13 $\mu m^2\ s^{-1}$ i *E. coli*s cytoplasma. Vår metod kan användas för att studera diffusionen av intracellulära partiklar som kan märkas med mEos2 och har höga kopietal.

Den optiska uppställningen byggdes kring ett mikroskop som var utrustat med ett oljeobjektiv och en känslig kamera. Vi kontrollerade mikroskopet och kameran med det kommersiella programmet MetaMorph. En excitationslaser och en fotoomvandlingslaser leddes in i mikroskopet med hjälp av en dikroisk spegel. Vi kontrollerade fotomvandlingsbelysningen med en slutare.

Celler som uttryckte mEos2 från en plasmid odlades övernatt vid 37 °C i minimalt medium som innehöll aminosyror och glukos. Cellerna späddes ut tusen gånger i färskt medium, odlades vid 37 °C och placerades på en agaroskudde som innehöll färskt medium. Cellerna avbildades i en flödescell under några minuter vid 250 Hz vid rumstemperatur. Frekvensen för fotoomvandlingspulserna valdes manuellt så att medelantalet fluorescenta mEos2-molekyler vid ett givet ögonblick var mindre än ett.

Bilderna analyserades med det kommersiella programmet DiaTrack. DiaTrack detekterar partiklars bilder genom att hitta lokala intensitetsmaxima efter att användaren har angett ett tröskelvärde för intensiteten. Programmet kan bestämma partiklarnas positioner genom att anpassa deras bilder med symmetriska gaussfunktioner efter att användaren har angett gaussfunktionernas halvbredd. DiaTrack konstruerar därefter trajektorier genom att ansluta punkter från på varandra följande bilder efter att användaren har angett partiklarnas maximalt tillåtna *xy*-förflyttning.

Vi approximerade cellgeometrierna som cylindrar med halvklotformade ändar. I den här approximationen definieras geometrin av fem parametrar: cellens bredd, längd, vinkel, *x*-position och *y*-position. Vi bestämde parametrarna genom att plotta alla punkterna i trajektorierna och manuellt rita linjer längs cellernas kort- och långaxlar. Vi bestämde mEos2:s diffusionskoefficienter genom att jämföra mEos2:s medelkvadratförflyttningar med medelkvadratförflyttningar från trajektoriesimuleringar med olika diffusionskoefficienter och valde manuellt de diffusionskoefficienter som gav de bästa anpassningarna. Trajektorier simulerades genom att sampla *x*-, *y*- och *z*-förflyttningar på 10-µs-tidsskalan. Alla tre förflyttningar samplades om i de fall där *xyz*-förflyttningen flyttade partikeln utanför cellgeometrin. Vi samplade trajektoriernas startpunkter från jämna fördelningar i cellgeometrierna och tog hänsyn till positionernas osäkerheter genom att tillsätta brus till de simulerade trajektorierna.

Konfidensgränser för medelkvadratförflyttningar uppskattades med Monte Carlo-simuleringar. Vi använde konfidensintervallen för medelkvadratförflyttningarna för att avgöra om mEos2:s medelkvadratförflyttningar kunde förklaras med en modell där mEos2 diffunderar normalt i 13 $\mu m^2\ s^{-1}$ i alla cellerna. En konfidensnivå på 99 % användes för varje cell, vilket motsvarar en konfidensnivå på 95 % för de åtta cellerna.

Ribosomala subenheters rumsfördelning (delarbete II)

I delarbete II använde vi spårning av enskilda partiklar i levande *E. coli*-celler för att bestämma andelen fria ribosomala subenheter, klassificera enskilda subenheter som fria eller mRNA-bundna, och bestämma graden av uteslutning för bundna och fria subenheter var för sig. Vi visade att fria subenheter inte är uteslutna från nukleoiden. Den här upptäckten antyder starkt att translation av gryende mRNA:n kan starta i hela nukleoiden, vilket förlikar rumsseparationen av DNA och ribosomer med kotranskriptionell proteinsyntes. Vi visade också att fria subenhetsprekursorer är delvis uteslutna från den kompakterade nukleoiden efter att proteinsyntesen har hämmats. Den här upptäckten indikerar att det är aktiv proteinsyntes som normalt tillåter att ribosomala subenheter sätts ihop på gryende mRNA:n i hela nukleoiden och att effekterna av proteinsynteshämmare förstärks av de ribosomala subenheternas begränsade tillgång till gryende mRNA:n i den kompakterade nukleoiden.

Den optiska uppställningen byggdes kring ett mikroskop som var utrustat med ett oljeobjektiv och en känslig kamera. Vi kontrollerade mikroskopet och kameran med MetaMorph. En excitationslaser och en fotoomvandlingslaser leddes in i mikroskopet med hjälp av en dikroisk spegel. Vi kontrollerade fotomvandlingsbelysningen med en slutare.

För att kunna spåra ribosomala subenheter konstruerade vi *E. coli*-stammar som utrycker de ribosomala proteinerna L1 och S2 som fusioner till mEos2 från sina endogena lokus. Detta innebär att varje L1- eller S2-protein ersätts med ett L1- eller S2-mEos2-protein. Cellerna odlades vid rumstemperatur i minimalt medium som innehöll aminosyror och glukos. De placerades på en agaroskudde som innehöll färskt medium och avbildades i en flödescell under 5 min vid 10, 50 eller 200 Hz vid rumstemperatur. I vissa av experimenten behandlade vi cellerna med 200 $\mu g\ ml^{-1}$ erytromycin eller rifampicin under 3 h och placerade cellerna på en agaroskudde som innehöll färskt medium och 200 $\mu g\ ml^{-1}$ av samma antibiotikum.

Vi detekterade partiklarnas bilder med en waveletsegmenteringsalgoritm och bestämde partiklarnas positioner genom att anpassa deras bilder med elliptiska gaussfunktioner. Antalet falska positiva punkter reducerades genom att endast behålla punkter som uppfyllde vissa krav. Vi korrigerade

också för drift genom att beräkna medeldrifthastigheter från ljusmikroskopibilder som var tagna före och efter fluorescensbilderna.

Cellgeometrierna approximerades som cylindrar med halvklotformade ändar och bestämdes från ljusmikroskopibilder eller enskilda ribosomala subenheters positioner. Vi konstruerade trajektorierna genom att ansluta punkter från på varandra följande bilder och behöll de trajektorier som bestod av minst fem punkter. Trajektorierna analyserades därefter genom att beräkna apparenta diffusionskoefficienter från medelkvadratförflyttningar över 5, 20 eller 100 ms. Vi bestämde andelen fria ribosomala subenheter genom att behandla varje fördelning av apparenta diffusionkoefficienter i de obehandlade cellerna som summan av en okänd fördelning för de mRNA-bundna subenheterna och en känd fördelning i de rifampicin-behandlade cellerna, där alla ribosomala subenheter är fria. Andelarna användes därefter för att bestämma tröskelvärden för de enskilda subenheternas apparenta diffusionskoefficienter. Vi använde tröskelvärdena för att klassificera varje subenhet i de obehandlade cellerna som bunden eller fri. Klassificeringsprecisionerna för de individuella subenheterna uppskattades genom att klassificera subenheterna i de rifampicin-behandlade cellerna, där alla ribosomala subenheter är fria.

För att kunna bestämma partiklarnas medelrumsfördelning beräknade vi deras relativa kortaxelpositioner. Vi bestämde rumsfördelningarna genom att representera de relativa kortaxelpositionerna från de cylindriska delarna av cellerna med normerade gaussfunktioner med standardavvikelser som motsvarar standardosäkerheterna för de relativa kortaxelpositionerna. För att kunna bestämma graden av uteslutning och uppskatta ändringar i nukleoidens storlek härledde vi analytiska modeller för fördelningarna av de relativa kortaxelpositionerna i de cylindriska delarna av cellerna. I de här modellerna är partiklarna antingen inuti eller utanför en cylinder med okänd radie i mitten av cellen. Vi tog hänsyn till positioneras osäkerheter genom att falta de härledda fördelningarna med normerade gaussfunktioner med standardavvikelser som motsvarar de relativa kortaxelpositionernas medelstandardosäkerheter. Trajektorier simulerades i cylindrar med halvklotformade ändar för att avgöra om trajektorieklassificeringen är robust trots att trajektorierna består av relativt få punkter. Vi simulerade också trajektorier i klot för att bestämma graden av instängning för bundna och fria ribosomala subenheter.

Author's contributions

Paper I

I constructed a *relA* knockout strain, participated in the mEos2 tracking experiments, performed bulk growth experiments, analyzed the mEos2 trajectories, performed the trajectory simulations, helped draft the manuscript and edited subsequent versions of the manuscript.

Paper II

I helped build the optical setup, constructed bacterial strains, performed the agarose pad experiments and the trajectory simulations, analyzed the agarose pad data, drafted the manuscript and edited subsequent versions of the manuscript.

Acknowledgements

I would like to thank

- my supervisor Johan for giving me the opportunity to perform the research and helping me become a better scientist, finish the investigations and my graduate studies, and improve my manuscripts and thesis
- my co-supervisor Måns for sharing his wisdom
- Brian for his significant contributions to the first investigation
- Fredrik for his significant contributions to the second investigation
- David for helpful discussions and comments on my manuscripts and thesis, and his contributions to the second investigation
- my other coauthors for their contributions to the investigations
- Cia for helpful discussions and comments on my manuscripts
- Prune for answering my questions, constructing plasmids and strains, managing the laboratory and playing good music
- Irmeli for organizing events and providing administrative assistance
- Anel for being frank and friendly
- Mats for being friendly and helpful
- Petter for being a good friend and sharing his wisdom
- other members of the Elf laboratory and the RiboCORE consortium for helpful discussions
- my parents and my sister for helpful comments on my thesis and their support.

References

1. Crick F (1970) Central dogma of molecular biology. *Nature* 227(5258):561–563.
2. Reid G, Howard J, Gan BS (2001) Can bacterial interference prevent infection? *Trends Microbiol* 9(9):424–428.
3. Conly JM, Stein K (1992) The production of menaquinones (vitamin K2) by intestinal bacteria and their role in maintaining coagulation homeostasis. *Prog Food Nutr Sci* 16(4):307–343.
4. Volkmer B, Heinemann M (2011) Condition-dependent cell volume and concentration of *Escherichia coli* to facilitate data conversion for systems biology modeling. *Plos One* 6(7):e23126.
5. Berg HC, Brown DA (1972) Chemotaxis in *Escherichia coli* analysed by three-dimensional tracking. *Nature* 239(5374):500–504.
6. Blattner FR, et al. (1997) The complete genome sequence of *Escherichia coli* K-12. *Science* 277(5331):1453–1462.
7. Reshes G, Vanounou S, Fishov I, Feingold M (2008) Timing the start of division in *E. coli*: a single-cell study. *Phys Biol* 5(4):046001.
8. Helmstetter CE (1968) DNA synthesis during the division cycle of rapidly growing *Escherichia coli* B/r. *J Mol Biol* 31(3):507–518.
9. Neidhardt FC, Umbarger HE (1996) Chemical composition of *Escherichia coli*. *Escherichia coli and Salmonella: Cellular and Molecular Biology*, ed Neidhardt FC (Am. Soc. Microbiol., Washington, DC), Vol 1, pp 13–16.
10. Ishihama Y, et al. (2008) Protein abundance profiling of the Escherichia coli cytosol. *BMC Genomics* 9:102.
11. Kamihira M, Taniguchi M, Kobayashi T (1987) Sterilization of microorganisms with supercritical carbon dioxide. *Agric Biol Chem* 51(2):407–412.
12. Fisher JK, et al. (2013) Four-dimensional imaging of *E. coli* nucleoid organization and dynamics in living cells. *Cell* 153(4):882–895.
13. Azam TA, Iwata A, Nishimura A, Ueda S, Ishihama A (1999) Growth phase-dependent variation in protein composition of the *Escherichia coli* nucleoid. *J Bacteriol* 181(20):6361–6370.
14. Wang W, Li GW, Chen C, Xie XS, Zhuang X (2011) Chromosome organization by a nucleoid-associated protein in live bacteria. *Science* 333(6048):1445–1449.
15. Weinstein-Fischer D, Altuvia S (2007) Differential regulation of *Escherichia coli* topoisomerase I by Fis. *Mol Microbiol* 63(4):1131–1144.
16. Leonard AC, Grimwade JE (2005) Building a bacterial orisome: emergence of new regulatory features for replication origin unwinding. *Mol Microbiol* 55(4):978–985.
17. Grainger DC, Hurd D, Goldberg MD, Busby SJW (2006) Association of nucleoid proteins with coding and non-coding segments of the *Escherichia coli* genome. *Nucleic Acids Res* 34(16):4642–4652.

18. Claret L, Rouviere-Yaniv J (1997) Variation in HU composition during growth of *Escherichia coli*: the heterodimer is required for long term survival. *J Mol Biol* 273(1):93–104.
19. Oberto J, Nabti S, Jooste V, Mignot H, Rouviere-Yaniv J (2009) The HU regulon is composed of genes responding to anaerobiosis, acid stress, high osmolarity and SOS induction. *Plos One* 4(2):e4367.
20. van Noort J, Verbrugge S, Goosen N, Dekker C, Dame RT (2004) Dual architectural roles of HU: Formation of flexible hinges and rigid filaments. *Proc Natl Acad Sci USA* 101(18):6969–6974.
21. Oshima T, Ishikawa S, Kurokawa K, Aiba H, Ogasawara N (2006) *Escherichia coli* histone-like protein H-NS preferentially binds to horizontally acquired DNA in association with RNA polymerase. *DNA Res* 13(4):141–153.
22. Zhang A, Rimsky S, Reaban ME, Buc H, Belfort M (1996) *Escherichia coli* protein analogs StpA and H-NS: regulatory loops, similar and disparate effects on nucleic acid dynamics. *Embo J* 15(6):1340–1349.
23. Spurio R, et al. (1992) Lethal overproduction of the *Escherichia coli* nucleoid protein H-NS: ultramicroscopic and molecular autopsy. *Mol Gen Genet* 231(2):201–211.
24. Macchi R, et al. (2003) Recruitment of σ^{54}-RNA polymerase to the *Pu* promoter of *Pseudomonas putida* through integration host factor-mediated positioning switch of α subunit carboxyl-terminal domain on an UP-like element. *J Biol Chem* 278(30):27695–27702.
25. Santero E, et al. (1992) Role of integration host factor in stimulating transcription from the σ^{54}-dependent *nifH* promoter. *J Mol Biol* 227(3):602–620.
26. Mangan MW, et al. (2006) The integration host factor (IHF) integrates stationary-phase and virulence gene expression in *Salmonella enterica* serovar Typhimurium. *Mol Microbiol* 59(6):1831–1847.
27. Kelman Z, O'Donnell M (1995) DNA polymerase III holoenzyme: structure and function of a chromosomal replicating machine. *Annu Rev Biochem* 64:171–200.
28. Wu YH, Franden MA, Hawker JR, Jr., McHenry CS (1984) Monoclonal antibodies specific for the α subunit of the *Escherichia coli* DNA polymerase III holoenzyme. *J Biol Chem* 259(19):12117–12122.
29. Studwell PS, O'Donnell M (1990) Processive replication is contingent on the exonuclease subunit of DNA polymerase III holoenzyme. *J Biol Chem* 265(2):1171–1178.
30. Bakshi S, Siryaporn A, Goulian M, Weisshaar JC (2012) Superresolution imaging of ribosomes and RNA polymerase in live *Escherichia coli* cells. *Mol Microbiol* 85(1):21–38.
31. Vogel U, Jensen KF (1994) The RNA chain elongation rate in *Escherichia coli* depends on the growth rate. *J Bacteriol* 176(10):2807–2813.
32. Melnikov S, et al. (2012) One core, two shells: bacterial and eukaryotic ribosomes. *Nat Struct Mol Biol* 19(6):560–567.
33. Young R, Bremer H (1976) Polypeptide-chain-elongation rate in *Escherichia coli* B/r as a function of growth rate. *Biochem J* 160(2):185–194.
34. Proshkin S, Rahmouni AR, Mironov A, Nudler E (2010) Cooperation between translating ribosomes and RNA polymerase in transcription elongation. *Science* 328(5977):504–508.
35. Yanofsky C (1981) Attenuation in the control of expression of bacterial operons. *Nature* 289(5800):751–758.
36. Richardson JP (1991) Preventing the synthesis of unused transcripts by Rho factor. *Cell* 64(6):1047–1049.

37. Hobot JA, et al. (1985) Shape and fine structure of nucleoids observed on sections of ultrarapidly frozen and cryosubstituted bacteria. *J Bacteriol* 162(3):960–971.
38. Campos M, Jacobs-Wagner C (2013) Cellular organization of the transfer of genetic information. *Curr Opin Microbiol* 16(2):171–176.
39. Wehrli W, Knüsel F, Schmid K, Staehelin M (1968) Interaction of rifamycin with bacterial RNA polymerase. *Proc Natl Acad Sci USA* 61(2):667–673.
40. Campbell EA, et al. (2001) Structural mechanism for rifampicin inhibition of bacterial RNA polymerase. *Cell* 104(6):901–912.
41. Blundell MR, Wild DG (1971) Altered ribosomes after inhibition of *Escherichia coli* by rifampicin. *Biochem J* 121(3):391–398.
42. Mao JC-H, Putterman M (1969) The intermolecular complex of erythromycin and ribosome. *J Mol Biol* 44(2):347–361.
43. Pestka S (1974) Binding of [^{14}C]Erythromycin to *Escherichia coli* ribosomes. *Antimicrob Agents Chemother* 6(4):474–478.
44. Moazed D, Noller HF (1987) Chloramphenicol, erythromycin, carbomycin and vernamycin B protect overlapping sites in the peptidyl transferase region of 23S ribosomal RNA. *Biochimie* 69(8):879–884.
45. Andersson S, Kurland CG (1987) Elongating ribosomes *in vivo* are refractory to erythromycin. *Biochimie* 69(8):901–904.
46. Siibak T, et al. (2009) Erythromycin- and chloramphenicol-induced ribosomal assembly defects are secondary effects of protein synthesis inhibition. *Antimicrob Agents Chemother* 53(2):563–571.
47. Siibak T, et al. (2011) Antibiotic-induced ribosomal assembly defects result from changes in the synthesis of ribosomal proteins. *Mol Microbiol* 80(1):54–67.
48. Betzig E, et al. (2006) Imaging intracellular fluorescent proteins at nanometer resolution. *Science* 313(5793):1642–1645.
49. Hess ST, Girirajan TPK, Mason MD (2006) Ultra-high resolution imaging by fluorescence photoactivation localization microscopy. *Biophys J* 91(11):4258–4272.
50. Manley S, et al. (2008) High-density mapping of single-molecule trajectories with photoactivated localization microscopy. *Nat Methods* 5(2):155–157.
51. Niu L, Yu J (2008) Investigating intracellular dynamics of FtsZ cytoskeleton with photoactivation single-molecule tracking. *Biophys J* 95(4):2009–2016.
52. Shimomura O, Johnson FH, Saiga Y (1962) Extraction, purification and properties of aequorin, a bioluminescent protein from the luminous hydromedusan, *Aequorea*. *J Cell Comp Physiol* 59(3):223–239.
53. Heim R, Tsien RY (1996) Engineering green fluorescent protein for improved brightness, longer wavelengths and fluorescence resonance energy transfer. *Curr Biol* 6(2):178–182.
54. Prasher DC, Eckenrode VK, Ward WW, Prendergast FG, Cormier MJ (1992) Primary structure of the *Aequorea victoria* green-fluorescent protein. *Gene* 111(2):229–233.
55. Chalfie M, Tu Y, Euskirchen G, Ward WW, Prasher DC (1994) Green fluorescent protein as a marker for gene expression. *Science* 263(5148):802–805.
56. McKinney SA, Murphy CS, Hazelwood KL, Davidson MW, Looger LL (2009) A bright and photostable photoconvertible fluorescent protein. *Nat Methods* 6(2):131–133.

57. Wiedenmann J, et al. (2004) EosFP, a fluorescent marker protein with UV-inducible green-to-red fluorescence conversion. *Proc Natl Acad Sci USA* 101(45):15905–15910.
58. Jones SA, Shim S-H, He J, Zhuang X (2011) Fast, three-dimensional super-resolution imaging of live cells. *Nat Methods* 8(6):499-505.
59. Zhang M, et al. (2012) Rational design of true monomeric and bright photoactivatable fluorescent proteins. *Nat Methods* 9(7):727–729.
60. Hell SW, Wichmann J (1994) Breaking the diffraction resolution limit by stimulated emission: stimulated-emission-depletion fluorescence microscopy. *Opt Lett* 19(11):780–782.
61. Klar TA, Jakobs S, Dyba M, Egner A, Hell SW (2000) Fluorescence microscopy with diffraction resolution barrier broken by stimulated emission. *Proc Natl Acad Sci USA* 97(15):8206–8210.
62. Donnert G, et al. (2006) Macromolecular-scale resolution in biological fluorescence microscopy. *Proc Natl Acad Sci USA* 103(31):11440–11445.
63. Rust MJ, Bates M, Zhuang X (2006) Sub-diffraction-limit imaging by stochastic optical reconstruction microscopy (STORM). *Nat Methods* 3(10):793–795.
64. Terry BR, Matthews EK, Haseloff J (1995) Molecular characterisation of recombinant green fluorescent protein by fluorescence correlation microscopy. *Biochem Biophys Res Commun* 217(1):21–27.
65. Swaminathan R, Hoang CP, Verkman AS (1997) Photobleaching recovery and anisotropy decay of green fluorescent protein GFP-S65T in solution and cells: cytoplasmic viscosity probed by green fluorescent protein translational and rotational diffusion. *Biophys J* 72(4):1900–1907.
66. Partikian A, Ölveczky B, Swaminathan R, Li Y, Verkman AS (1998) Rapid diffusion of green fluorescent protein in the mitochondrial matrix. *J Cell Biol* 140(4):821–829.
67. Elowitz MB, Surette MG, Wolf P-E, Stock JB, Leibler S (1999) Protein mobility in the cytoplasm of *Escherichia coli*. *J Bacteriol* 181(1):197–203.
68. Konopka MC, Shkel IA, Cayley S, Record MT, Weisshaar JC (2006) Crowding and confinement effects on protein diffusion in vivo. *J Bacteriol* 188(17):6115–6123.
69. Weber SC, Spakowitz AJ, Theriot JA (2010) Bacterial chromosomal loci move subdiffusively through a viscoelastic cytoplasm. *Phys Rev Lett* 104(23):238102.
70. Weber SC, Spakowitz AJ, Theriot JA (2012) Nonthermal ATP-dependent fluctuations contribute to the in vivo motion of chromosomal loci. *Proc Natl Acad Sci USA* 109(19):7338–7343.
71. Parry BR, et al. (2014) The bacterial cytoplasm has glass-like properties and is fluidized by metabolic activity. *Cell* 156(1–2):183–194.
72. Magde D, Elson E, Webb WW (1972) Thermodynamic fluctuations in a reacting system — measurement by fluorescence correlation spectroscopy. *Phys Rev Lett* 29(11):705–708.
73. Axelrod D, Koppel DE, Schlessinger J, Elson E, Webb WW (1976) Mobility measurement by analysis of fluorescence photobleaching recovery kinetics. *Biophys J* 16(9):1055–1069.
74. Geerts H, et al. (1987) Nanovid tracking: a new automatic method for the study of mobility in living cells based on colloidal gold and video microscopy. *Biophys J* 52(5):775–782.
75. English BP, et al. (2011) Single-molecule investigations of the stringent response machinery in living bacterial cells. *Proc Natl Acad Sci USA* 108(31):E365–E373.

76. Uphoff S, Reyes-Lamothe R, Garza de Leon F, Sherratt DJ, Kapanidis AN (2013) Single-molecule DNA repair in live bacteria. *Proc Natl Acad Sci USA* 110(20):8063–8068.
77. Lakadamyali M, Rust MJ, Babcock HP, Zhuang X (2003) Visualizing infection of individual influenza viruses. *Proc Natl Acad Sci USA* 100(16):9280–9285.
78. Rust MJ, Lakadamyali M, Zhang F, Zhuang X (2004) Assembly of endocytic machinery around individual influenza viruses during viral entry. *Nat Struct Mol Biol* 11(6):567–573.
79. van der Schaar HM, et al. (2008) Dissecting the cell entry pathway of dengue virus by single-particle tracking in living cells. *Plos Pathog* 4(12):e1000244.
80. Golding I, Cox EC (2004) RNA dynamics in live *Escherichia coli* cells. *Proc Natl Acad Sci USA* 101(31):11310–11315.
81. Kim SY, Gitai Z, Kinkhabwala A, Shapiro L, Moerner WE (2006) Single molecules of the bacterial actin MreB undergo directed treadmilling motion in *Caulobacter crescentus*. *Proc Natl Acad Sci USA* 103(29):10929–10934.
82. Garner EC, et al. (2011) Coupled, circumferential motions of the cell wall synthesis machinery and MreB filaments in *B. subtilis*. *Science* 333(6039):222–225.
83. Domínguez-Escobar J, et al. (2011) Processive movement of MreB-associated cell wall biosynthetic complexes in bacteria. *Science* 333(6039):225–228.
84. van Teeffelen S, et al. (2011) The bacterial actin MreB rotates, and rotation depends on cell-wall assembly. *Proc Natl Acad Sci USA* 108(38):15822–15827.
85. Kao HP, Verkman AS (1994) Tracking of single fluorescent particles in three dimensions: use of cylindrical optics to encode particle position. *Biophys J* 67(3):1291–1300.
86. Juette MF, et al. (2008) Three-dimensional sub–100 nm resolution fluorescence microscopy of thick samples. *Nat Methods* 5(6):527–529.
87. Pavani SRP, Piestun R (2008) Three dimensional tracking of fluorescent microparticles using a photon-limited double-helix response system. *Opt Express* 16(26):22048–22057.
88. Mortensen KI, Churchman LS, Spudich JA, Flyvbjerg H (2010) Optimized localization analysis for single-molecule tracking and super-resolution microscopy. *Nat Methods* 7(5):377–381.
89. Ulbrich MH, Isacoff EY (2007) Subunit counting in membrane-bound proteins. *Nat Methods* 4(4):319–321.
90. Llopis PM, et al. (2010) Spatial organization of the flow of genetic information in bacteria. *Nature* 466(7302):77–81.
91. Datsenko KA, Wanner BL (2000) One-step inactivation of chromosomal genes in *Escherichia coli* K-12 using PCR products. *Proc Natl Acad Sci USA* 97(12):6640–6645.
92. Cherepanov PP, Wackernagel W (1995) Gene disruption in *Escherichia coli*: Tc^R and Km^R cassettes with the option of Flp-catalyzed excision of the antibiotic-resistance determinant. *Gene* 158(1):9–14.
93. Izeddin I, et al. (2012) Wavelet analysis for single molecule localization microscopy. *Opt Express* 20(3):2081–2095.
94. Parthasarathy R (2012) Rapid, accurate particle tracking by calculation of radial symmetry centers. *Nat Methods* 9(7):724–726.
95. Young JW, et al. (2012) Measuring single-cell gene expression dynamics in bacteria using fluorescence time-lapse microscopy. *Nat Protoc* 7(1):80–88.
96. Crawford R, et al. (2013) Long-lived intracellular single-molecule fluorescence using electroporated molecules. *Biophys J* 105(11):2439–2450.

97. Sustarsic M, et al. (2014) Optimized delivery of fluorescently labeled proteins in live bacteria using electroporation. *Histochem Cell Biol* 142(1):113–124.
98. Gebhardt JCM, et al. (2013) Single-molecule imaging of transcription factor binding to DNA in live mammalian cells. *Nat Methods* 10(5):421–426.

Acta Universitatis Upsaliensis

Digital Comprehensive Summaries of Uppsala Dissertations from the Faculty of Science and Technology 1159

Editor: The Dean of the Faculty of Science and Technology

A doctoral dissertation from the Faculty of Science and Technology, Uppsala University, is usually a summary of a number of papers. A few copies of the complete dissertation are kept at major Swedish research libraries, while the summary alone is distributed internationally through the series Digital Comprehensive Summaries of Uppsala Dissertations from the Faculty of Science and Technology. (Prior to January, 2005, the series was published under the title "Comprehensive Summaries of Uppsala Dissertations from the Faculty of Science and Technology".)

Distribution: publications.uu.se
urn:nbn:se:uu:diva-229342

ACTA
UNIVERSITATIS
UPSALIENSIS
UPPSALA
2014